*J. Fluid Mech.* (2007), *vol.* 582, *pp.* 23–52.  
doi:10.1017/S0022112007005794 Printed in the United Kingdom

# Shoreface-connected ridges under the action of waves and currents

EMILY M. LANE[1]† AND JUAN M. RESTREPO[2]

[1]Institute of Geophysics and Planetary Physics, University of California, Los Angeles, CA 90095-1567, USA

[2]Department of Mathematics and Department of Physics, University of Arizona, Tucson, AZ 85721, USA

(Received 18 January 2005 and in revised form 5 December 2006)

Up-current-rotated, shoreface-connected ridges are found in various coastal areas around the world. An often-quoted conjecture is that these ridges form during storm conditions through free instabilities in the erodible bed. Under these conditions both waves and currents are expected to play a significant role in the hydrodynamics. Although some existing models have included the effects of waves parametrically in their bottom friction terms and sediment equations, the dynamical effects of wave–current interaction have not been explored. In this paper we begin to rectify this by considering the effects of wave–current interaction on the bed-form instabilities of a simple model. This raises the possibility of unsteady alongshore flows and questions about the roles of wave parameters and boundary conditions, which we address here. We show that the flow is stable under the wave forcing; however the waves do affect the bed-form instability. The main dynamical effect of the waves is in altering the shapes of the unstable modes. Under various conditions, however, waves may enhance or suppress the instability or introduce new unstable modes. They also affect the celerity of the ridges. In addition, we investigate the mechanisms whereby the waves affect the instability. We also show a potential problem with the parameterization in terms of wave orbital velocity.

## 1. Introduction

Up-current-rotated, shoreface-connected ridges are found in certain coastal areas, such as off the east coast of North America (Duane *et al.* 1972; Swift *et al.* 1972), off the Dutch coast (van der Meene 1996) and off the Argentinian coast (Parker, Lanfredi & Swift 1982). These ridges form at angles of around 20°–35° to the shore, with the seaward side rotated upstream with respect to the landward side. They form in water 5–30 m deep. The ridges are spaced 5–10 km apart and can be several metres high. Most ridge evolution happens during large storms which drive alongshore currents on the order of 0.5 m $s^{-1}$. These storms occur several times a year at these locations, with durations from hours to days. In the case of the Dutch Coast, tidal currents are also significant but in the Mid-Atlantic Bight and off the coast of Argentina the role of tides is negligible. The ridges migrate downstream with a celerity of a few metres per year. Following Calvete, de Swart & Falques (2002) we consider the specific case of Long Island, USA, where the ridges are spaced approximately

† Present address: NIWA, PO Box 8602 Christchurch, New Zealand.

3.5 km apart, have a growth rate on the order of 100 years and a downstream celerity of around 2.3 m $yr^{-1}$.

The original supposition was that shoreface-connected ridges were sill-stands left over on the strand plain from the return of the Holocene sea (McClennen & McMaster 1971). However, their orientation, with the downshore end connected to the shoreface, does not fit with this conjecture unless the angle of the shoreline has changed significantly since then. Also, as these ridges are active under present day hydrodynamic conditions (Swift *et al.* 1978), they are not just a relic feature. Swift, Duane & McKinney (1973) hypothesized that the ridges are an erosional feature: storm-driven flows scour out the landward side of the shoreface-connected ridges; gradually the shoreline retreats, and as it does, the ridges migrate down-current and also offshore. A third hypothesis is that they form as instabilities of the erodible bed under the influence of the local hydraulic regime.

The idea that these ridges formed through a free instability was postulated by Trowbridge (1995), largely inspired by the work of Huthnance (1982) based on Off's (1960) observations of current-aligned ridges. Using a simple model where the evolution of the bottom topography is related to the divergence of the flow, Trowbridge (1995) shows that the unstable eigenfunctions are up-current-rotated ridges similar to those observed. Mass considerations mean that the alongshore flow is deflected offshore over the ridge crests. This deflection causes the flow to converge, which causes deposition and increases the height of the ridges. Thus up-current-rotated ridges can form from the instability of a smooth erodible bottom. Trowbridge's model, however, has no distinguished length scale to explain the size and spacing of the ridges.

Falques, Calvete & Montoto (1998*a*) and Falques *et al.* (1998*b*) extended Trowbridge's model by using two-dimensional shallow-water equations for the evolution of the currents and adding a diffusive term to the bottom-topography evolution equation. The diffusive term represents the proclivity of sand grains to move downslope. With these additions the model selects a distinguished length scale. The fastest growing mode, which often represents the length scale of the final feature, is chosen through a balance between the destabilizing effects of the convergence term and the stabilizing effects of the diffusion term. This model still has the problem, however, that the ratio between e-folding time scale and the celerity is unrealistic.

The basic model was modified by Calvete *et al.* (2001*a*) and later papers (Calvete *et al.* 2002; Walgreen, Calvete & de Swart 2002; Calvete & de Swart 2003; Walgreen, de Swart & Calvete 2003) to include both bed load and suspended load. Wave effects were also included parametrically in the bottom friction term and the sediment dynamics equations. These additions give more realistic ratios between the e-folding and migration time scales. Walgreen, de Swart & Calvete (2003, 2004) studied the morphological effects of allowing for different grain sizes. Calvete *et al.* (2001*b*) and Walgreen *et al.* (2002) considered both tides and steady currents. Finite-amplitude effects were explored in Calvete *et al.* (1999, 2002) and Calvete & de Swart (2003) with the overall conclusion that the outcome of the linear instability calculations was robust, at least qualitatively but that other modes in addition to the fastest growing mode were also important to the final bed-form shape.

Field observations (Duane *et al.* 1972; Swift *et al.* 1972; Parker *et al.* 1982) have shown that considerable ridge evolution occurs during storms. In such oceanic conditions both waves and currents are prominent in the hydrodynamics. Restrepo (2001) developed a coupled system of equations for the waves, currents and erodible bed by depth averaging the wave–current model in McWilliams & Restrepo (1999)

and deriving a mass conservation statement for the sediment consistent with the tracer evolution equation which takes into account waves and currents.

Restrepo (2001) considered the effect of waves on the linear instability results that utilized current-only models for the hydrodynamics. Furthermore, he attempted to check the crucial assumption of the adiabatic approximation which was exploited in Falques *et al.* (1998*b*) to suppress potential instabilities due to the hydrodynamics. However, the analysis of the wave effects on the shoreface-connected ridge model in was tentative, for two reasons: the linear wave dynamics interacted only weakly with the rotational flow and the bottom topography and, secondly, resolution constraints were impractical from a computational standpoint.

Here we take another look at how wave effects change the outcome of instability calculations involving current-only models for the shore-connected ridge problem. We do so armed with a much improved wave/current interaction model which was derived by revisiting the scaling, going to higher order and circumventing the small-scale resolution problem. This gives a much more complete and generally applicable model for wave–current interaction on the continental shelf. This model appears in McWilliams, Restrepo & Lane (2004, referred to hereinas MRL04).

With a dynamic model for the fully three-dimensional hydrodynamics and a suitable sediment evolution model it is now possible to explore the shoreface-connected ridge problem over time scales that encompass the variable forcing conditions. Moreover, our model is capable of handling the extreme temporal scales, encompassing the range from storm-driven flows to hydrodynamics over decades, and spatial scales of the order of tens of metres to tens of kilometres.

Before we can consider the transient problem, however, there are a number of fundamental issues related to the assumptions in the shoreface-connected ridge model that need to be addressed. This study will show how the shoreface-connected coupled sediment–ocean dynamics model is modified when waves are taken into account. Specifically, we consider (1) how the linear instability results on the shoreface-connected ridge problem change when waves are taken into account; (2) how these changes are manifested when wave parameters are varied. Furthermore, our consideration of wave–current interaction raised other issues. This paper also addresses: (3) the difference between fixing the perturbation at the shoreward boundary (Dirichlet boundary conditions) and imposing a no-flux (Neumann) boundary condition; (4) whether the adiabatic assumption is justified i.e. whether currents are steady, especially under wave forcing, and whether the solutions are significantly affected if the morphological and hydrodynamic time scales are not well separated; (5) what wave mechanisms affect the morphodynamics; and finally (6) we show a potential problem with parameterizing the sediment fluxes in terms of the wave orbital velocity.

## 2. Governing equations

Shoreface-connected ridges form in finite-depth water on the continental shelf. The peak of the wave spectrum has a wavelength of around 100 m giving $\mu = kH_0 \sim 1$, where $k$ is the wavenumber magnitude and $H_0$ is the characteristic depth of the water column. The ridges represent changes in bottom-topography elevation of metres over distances of kilometres. Thus their length scales are long compared with the typical length scale of the waves. The storm-driven currents have speeds on the order of 0.25–0.5 m s$^{-1}$ in microtidal regions (Calvete *et al.* 2001*a*) with comparable wave orbital speeds. This suggests that the asymptotic theory derived in MRL04 is valid in this setting.

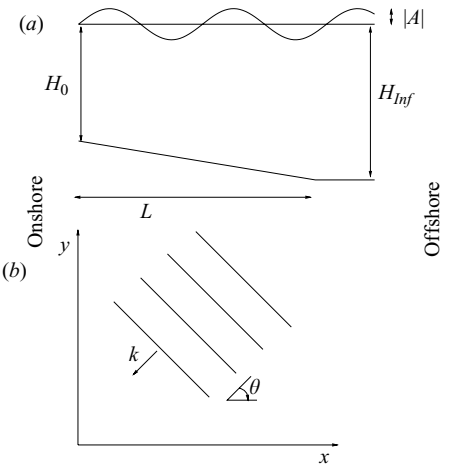


FIGURE 1. Schematic diagram of quantities used in the calculations (not to scale). (*a*) side view; (*b*) plan view.

We thus base our equations on those derived in MRL04. These equations represent a complete self-consistent model and include the full implications of the wave–current interactions on boundary conditions, tracer equations, etc. These equations also give the full wave dynamics, a problem which limited Restrepo (2001). The full implications of this substantially more complete and scale-appropriate model will only be seen when we consider the dynamic, storm-driven, time-dependent dynamics of the shoreface-connected ridges. This will include the long-wave contributions and multifrequency wave-spectrum wave trains. For the moment we limit considerations to the simpler case of the effect of a single wavetrain on the shoreface-connected ridges.

We consider a model domain that is semi-infinite in the $x$ (cross-shore) direction and periodic in the $y$ (longshore) direction. The model does not take into account the surf zone so that $x = 0$ should not be considered as the shore *per se* but rather the shorewardmost part of the domain.

### 2.1. *Waves*

We assume monochromatic waves at the peak of the spectrum with wavenumber, $\boldsymbol{k} = -(k\cos(\theta), k\sin(\theta))$, amplitude $A$ and frequency $\sigma$ (see figure 1). The group velocity of the waves is $\boldsymbol{C}_g$. Quiescent ocean level is $Z = 0$ with the ocean bottom at $Z = -H$. The waves propagate according to the equations (see MRL04)

$$\frac{\partial \boldsymbol{k}}{\partial t} + \boldsymbol{C}_g \cdot \nabla_\perp \boldsymbol{k} = -\frac{k\sigma}{\sinh[2kH]} \nabla_\perp H,$$

$$\frac{\partial \sigma}{\partial t} + \boldsymbol{C}_g \cdot \nabla_\perp \sigma = 0,$$

$$\frac{\partial |A|^2}{\partial t} + \nabla_\perp \cdot (\boldsymbol{C}_g |A|^2) = 0.$$

Time is $t$ and $\nabla_\perp = (\partial/\partial x, \partial/\partial y)$ is the horizontal derivative. The frequency is related to the scalar wavenumber through $\sigma^2 = gk\tanh(kH)$. Note that these equations agree to lowest order with the standard equations in Mei (1989) given the scaling assumption made in MRL04. For convenience we rewrite the wavenumber equations in terms of

the scalar wavenumber $k$ and the angle of the waves $\theta$ with respect to the $x$-axis:

$$\frac{\partial k}{\partial t} + \boldsymbol{C}_g \cdot \nabla_\perp k = \frac{\sigma k}{\sinh(2kH)} \left( \cos(\theta) \frac{\partial H}{\partial x} + \sin(\theta) \frac{\partial H}{\partial y} \right),$$
$$\frac{\partial \theta}{\partial t} + \boldsymbol{C}_g \cdot \nabla_\perp \theta = -\frac{\sigma}{\sinh(2kH)} \left( \sin(\theta) \frac{\partial H}{\partial x} - \cos(\theta) \frac{\partial H}{\partial y} \right).$$

Note that the scalar wavenumber evolution is dependent only upon the bottom-topography gradient parallel to the direction of the waves, whereas the wave-angle evolution depends only upon the bottom-topography gradient perpendicular to the wave direction.

The wave quantities will be specified in the far field ($x \to \infty$) and we assume a radiation boundary condition at $x = 0$. This is commensurate with the waves passing through this domain and then being dissipated through breaking closer to shore in the surf zone.

### 2.2. *Currents*

We derive shallow water equations from MRL04, §9 by vertically integrating the horizontal momentum equations (MRL04, (9.15)) and using the continuity equation (MRL04, (9.2)), boundary conditions (MRL04, (9.3), (9.9), (9.12)) and the vertical momentum equation (MRL04, (9.17)). We assume that vertical variations in velocity are negligible (see MRL04, §12 for a general discussion and also Lentz (2001) for the situation at the coast at North Carolina). We add surface and bottom forcing terms. This gives the vertically integrated horizontal momentum equation

$$\frac{\partial \boldsymbol{V}}{\partial t} + \boldsymbol{V} \cdot \nabla_\perp \boldsymbol{V} + f \hat{\boldsymbol{Z}} \times \boldsymbol{V} + g \nabla_\perp \zeta^c = -g \nabla_\perp \mathscr{G} - \hat{\boldsymbol{Z}} \times \boldsymbol{V}^{St} (\chi^c + f) + \frac{\boldsymbol{\tau} - r(x) \boldsymbol{V}}{H + \zeta^c}. \quad (2.1)$$

$\boldsymbol{V} = (U, V)$ is the vertically averaged current, $\chi^c = \hat{\boldsymbol{Z}} \cdot (\nabla_\perp \times \boldsymbol{V})$ the vertical vorticity, $\zeta^c$ is the mean sea elevation (averaged over the waves), $\boldsymbol{V}^{St} = g|A|^2/(2\sigma H)\boldsymbol{k} = (U^{St}, V^{St})$ is the vertically averaged Stokes drift. (This expression for the vertically averaged Stokes drift corrects an obvious typographical error in Restrepo (2001).) The Coriolis parameter is $f$, acceleration due to gravity is $g$; $\mathscr{G}$ is a Bernoulli-head wave forcing term that combines wave effects on the pressure and sea elevation as well as the ambient pressure (further details are given in MRL04). It causes a form of wave set-up in the mean sea elevation. In the vertically averaged case $\mathscr{G}$ can be evaluated as

$$\mathscr{G} = \left\langle \frac{|A|^4 k^3}{2 \sinh(2kH)} \left( \frac{1}{2} + \tanh^2(kH) - \sinh^2(kH) + \frac{9}{16 \sinh^6(kH)} + \frac{9}{4 \sinh^2(kH)} \right) \right\rangle - \left\langle \frac{|A|^2 k \tanh(kH) \boldsymbol{k} \cdot \boldsymbol{V}}{\sigma} \right\rangle. \quad (2.2)$$

The vortex force term

$$-\hat{\boldsymbol{Z}} \times \boldsymbol{V}^{St} (\chi^c + f)$$

captures the effect of vorticity transferred to the waves through the action of the rotational currents and from planetary rotation. The effect of the wind is represented by a kinetic surface stress $\boldsymbol{\tau}$. We assume that the bed shear stress is linear in $\boldsymbol{V}$. It is more common to use a quadratic term in $\boldsymbol{V}$; however Falques *et al.* (1998*a*) showed that this makes minimal difference to the results. The coefficient of friction $r$ is proportional to the wave orbital velocity at the bottom, i.e. $r = \hat{r}|u^w|$.

The fluid mass conservation equation is

$$\frac{\partial}{\partial t}(\zeta^c + H) + \nabla_\perp \cdot ((H + \zeta^c)(\boldsymbol{V} + \boldsymbol{V}^{St})) = 0. \tag{2.3}$$

Unlike Restrepo (2001), here we include the tendency term $\partial H/\partial t$ in equation (2.3). The bottom topography changes over time scales that are appreciably slower than the time scales associated with changes in surface elevation, thus $\partial H/\partial t$ can be thought of as a perturbation to (2.3). Over short time scales, the surface elevation balances with the divergence of the vertically integrated mass flux. Over long times scales, however, the bottom topography changes. The sea surface elevation then adjusts slightly to take this into account.

To ensure that there is no net flux of water out of the shoreward side of the domain we assume that the Eulerian velocity balances the Stokes flow in the cross-shore direction, i.e.

$$U(x = 0) + U^{St}(x = 0) = 0.$$

We have a no stress boundary on $V$ at $x = 0$. At the outer boundary, we assume that all quantities are finite for $x \to \infty$.

The conservative wave effects on the currents are completely characterized by the vortex force, Bernoulli head and Stokes drift terms. Passive tracers are also advected by the Stokes drift in addition to the current. As discussed in MRL04 and Lane, Restrepo & McWilliams (2007) this is an alternative to the radiation stress parameterization. If wave effects, which enter explicitly through the Stokes drift velocity $\boldsymbol{V}^{St}$ and the Bernoulli head $\mathscr{G}$, are suppressed, we then obtain the standard shallow-water current equations. The vortex force and the Stokes drift terms are related in that they both represent advection by the Stokes drift (in the case of the vortex force it is advection of vorticity). The Bernoulli head term adjusts the pressure due to the waves and causes a small change in the mean sea elevation. Its effect on the evolution of the bottom topography is small and could possibly be left out of future work.

### 2.3. *Bottom topography*

The sediment dynamics equation for $\partial H/\partial t$ is

$$\frac{\partial H}{\partial t} = \nabla_\perp \cdot \boldsymbol{Q}, \tag{2.4}$$

where $\boldsymbol{Q}$ is the sediment transport. We adopt a sediment flux model similar to that of Calvete *et al.* (2002) and Walgreen *et al.* (2002), composed of a bed-load and a suspended-load term

$$\boldsymbol{Q} = \frac{\mu}{(1-p)}(\boldsymbol{Q}^b + \boldsymbol{Q}^s);$$

$\mu \approx 0.05$ is the fraction of the time there are storms around Long Island and $p \approx 0.4$ is the porosity of the bed.

The bed-load term is modelled by

$$\boldsymbol{Q}^b = \nu_b(|u_w|^2(\boldsymbol{v} + \boldsymbol{v}^{St}) - \lambda_b|u_w|^3\nabla h), \tag{2.5}$$

and the suspended-load term is modelled by

$$\boldsymbol{Q}^s = \nu_s(H|u_w|^3(\boldsymbol{v} + \boldsymbol{v}^{St}) - \lambda_s|u_w|^5\nabla h). \tag{2.6}$$

Both these terms include a component due to the divergence of the Lagrangian current and a diffusion term that represents the tendency of sand to form smooth structures. The waves affect the bottom-topography evolution equation in two ways. First, as

tracers are advected by the Stokes drift in addition to the Eulerian velocity, we must also take this into consideration in the model (see MRL04). Secondly, the waves act as an agent for bottom stirring, with the coefficients in the bed- and suspended-load terms being proportional to powers of the wave orbital velocity $|u_w|$ (see Calvete *et al.* 2002). The average orbital wave velocity at the bottom of the water column is

$$\langle |u_w| \rangle = \left\langle \frac{\sigma |A|}{\sinh(kH)} \right\rangle. \tag{2.7}$$

Note that this differs from previous papers (Calvete *et al.* 2002; Walgreen *et al.* 2002), where the wave orbital velocity was parametrized as a function of bottom topography through a shoaling formula.

For convenience, we rewrite (2.4) as

$$\frac{1}{\alpha}\frac{\partial H}{\partial t} = \tilde{Q}^b + \delta_{sb}\tilde{Q}^s, \tag{2.8}$$

where $\alpha = T_h/T_{mb}$ is the ratio of the hydrological time scale, $T_h = L/U_0$, and the morphological time scale of the bed-load transport,

$$T_{mb} = \frac{(1-p)}{\mu}\frac{H_0 L}{Q_0^b} = \frac{(1-p)}{\mu}\frac{H_0 L}{\nu_b U_{w0}^2 U_0}.$$

$U_0$ is the characteristic current speed, $U_{w0}$ is the characteristic wave orbital velocity, $H_0$ is the characteristic depth, $L$ is the characteristic horizontal length scale and $Q_0^b$ is the characteristic bed-load sediment transport. $\tilde{Q}^b = H_0/(\nu_b U_{w0}^2)Q^b$ and $\tilde{Q}^s = 1/(\nu_s U_{w0}^3)Q^s$ are the sediment transports multiplied by the ratio of the characteristic mass transport to the respective characteristic sediment transports. $\delta_{sb} = T_{mb}/T_{ms} = \nu_s U_{w0} H_0/\nu_b$ is the ratio of the morphological time scales of the bed-load transport to the suspended-load transport.

Although there are more complicated sediment dynamics models (see for example Walgreen *et al.* (2003, 2004), which include additional effects such as differing grain sizes) this model contains the essential features that reproduce the expected estimates for the ridge celerity and spacing. Moreover, the simplicity of this model allows the effects of the waves on the model to be more clearly discerned.

The above model includes the several different effects of waves. Two of these, namely their effect on the bottom friction of the current and as an agent for bottom stirring in the sediment model, have been included in previous models (Calvete *et al.* 2002; Walgreen *et al.* 2002) (although, as we mention in § 5.4 and Appendix A, they do not consider the full effect of these terms on the instability). The direct conservative effects of the waves on the current (either through addition of the vortex force and Bernoulli head or the radiation/interaction stress) has not previously been included in a model of shoreface-connected ridge formation, nor has the fact that tracers are advected by the Lagrangian current (i.e. the Eulerian current plus the Stokes drift) rather than the Eulerian current alone.

## 3. Reference state

We derive a steady-state solution to the equations of hydrodynamics and sediment motion, consistent with Calvete *et al.* (2002), which includes the conservative wave effects.

Our reference bottom topography is independent of $y$. It increases linearly from a depth of $H_0$ at $x = 0$ to $H_\infty$ over a distance $L$ and is flat thereafter. We smooth the

bottom around $x = L$. This avoids a jump discontinuity in the derivative that causes Gibbs oscillations in the spectral representation of the eigenvalue problem. As in Calvete *et al.* (2002), we use parameter values consistent with Long Island which give $H_0 = 14\,\mathrm{m}$, $H_\infty = 20\,\mathrm{m}$ and $L = 5.5\,\mathrm{km}$.

### 3.1. *Waves*

We assume that the far-field boundary condition for the incoming waves is steady and independent of $y$. As the reference bottom topography is also independent of $y$, the incoming reference wave varies only in $x$. The frequency $\sigma$ is constant throughout the domain. The scalar wavenumber $k(x)$ is obtained from the water depth $H(x)$ using the implicit relationship $\sigma^2 = gk(x)\tanh(k(x)H(x))$. $\theta$ and $|A|^2$ are found by solving the relationships

$$\frac{\partial \theta}{\partial x} = \frac{\sigma \tan(\theta(x))}{|\boldsymbol{C}_g| \sinh(k(x)H(x))} \frac{\partial H}{\partial x},$$

$$|A|^2(x) = \frac{|\boldsymbol{C}_{g\infty}| \cos(\theta_\infty)}{|\boldsymbol{C}_g(x)| \cos(\theta(x))} |A|^2_\infty,$$

where $\boldsymbol{C}_{g\infty}$, $\theta_\infty$ and $|A|^2_\infty$ are the group velocity, angle, and amplitude-squared of the incident waves in the far field, respectively. Because the vertically averaged Stokes drift is a wave quantity, its reference state is also independent of $y$.

Unless stated otherwise we assume an orbital velocity $\sigma = 0.63\,\mathrm{s}^{-1}$ and an incoming wave height of 0.8 m. This gives a wavenumber around $0.055\,\mathrm{m}^{-1}$, wave orbital velocity on the order of $50\,\mathrm{cm\,s}^{-1}$ and a Stokes drift on the order of $2\,\mathrm{cm\,s}^{-1}$.

### 3.2. *Currents*

We assume that a steady wind stress acts only in the $y$-direction and $\boldsymbol{\tau} = (0, \tau_y)$. We also assume that the sea elevation includes a small linear alongshore variation representing a pressure gradient that drives the alongshore flow, $\zeta^c = \xi(x) + sy$. Consistent with Long Island we take $\tau_y = -0.0004\,\mathrm{m^2\,s^{-2}}$ and $s = 2 \times 10^{-7}\,\mathrm{m\,m^{-1}}$. Thus, the alongshore velocity is forced by a wind in the negative $y$-direction and a pressure gradient. As $\tau_y$ and $s$ are oppositely signed the two forces act in unison. In this case the wind stress is the primary driver of the current, with the pressure gradient only playing a secondary role. This value of $\tau$ represents a wind of $11.5\,\mathrm{m\,s}^{-1}$ at 10 m according to the formula in Csanady (1982). Over the length scales of interest the sea elevation only varies by at most a centimetre and so is small compared to the water depth. This justifies assuming $H + \zeta^c \approx H$ in most cases.

Apart from the pressure gradient we assume that all other reference-state current variables are independent of $y$. In the cross-shore direction we assume a simple anti-Stokes flow, i.e. $U(x) = -U^{St}(x)$. Given these assumptions, we may calculate the alongshore reference velocity $V(x)$ from the longshore momentum equation (2.1),

$$V(x) = \frac{\tau_y - gsH(x)}{r(x)}.$$

Thus the offshore velocity is of the order of $U \sim 2\,\mathrm{cm\,s}^{-1}$ and the alongshore velocity is of the order $V \sim 40\,\mathrm{cm\,s}^{-1}$.

The sea elevation is determined by the cross-shore ($x$) component of (2.1),

$$\frac{\partial}{\partial x}\left(g\xi + g\mathscr{G} + \frac{U^{St2}}{2}\right) = f(V + V^{St}) + V^{St}\frac{\partial V}{\partial x} + \frac{rU^{St}}{H},$$

where $\xi(x)$ is chosen so as to balance these terms. Over the area of interest $\xi$ varies over a couple of centimetres.

These values give sediment fluxes of the order of $Q_b \sim 2 \times 10^{-5}\,\mathrm{m^2\,s^{-1}}$ and $Q_s \sim 1 \times 10^{-4}\,\mathrm{m^2\,s^{-1}}$, in line with the values reported in Calvete *et al.* (2002). The morphologic time scales are $T_{ms} \sim 60$ years and $T_{mb} \sim 1600$ years while the hydrologic time scale is of the order of a few hours.

## 4. Linear stability analysis

### 4.1. *Linear perturbation*

The steady state is perturbed according to

$$(U, V) = (-U^{St}(x) + u, V(x) + v), \qquad \zeta^c = \zeta^c(x, y) + z, \qquad H = H(x) - h.$$

The bottom perturbation, $h$, also perturbs the waves:

$$\theta = \theta(x) + o, \qquad k = k(x) + p, \qquad |A|^2 = |A|^2(x) + q.$$

In the same manner that the wavenumber may be obtained from the bottom topography, the wavenumber perturbation, $p$, is enslaved to the bottom perturbation. The linear relationship between the two is $p = -(\partial k/\partial H)h$, where

$$\frac{\partial k}{\partial H} = -\frac{2k^2}{\sinh(2kH) + 2kH}.$$

Linearizing the equations for the wave-angle perturbation, $o$, and the wave amplitude perturbation, $q$, gives

$$\frac{\partial o}{\partial t} = \mathscr{W}_{oo}o + \mathscr{W}_{oh}h, \quad \frac{\partial q}{\partial t} = \mathscr{W}_{qo}o + \mathscr{W}_{qq}q + \mathscr{W}_{qh}h, \tag{4.1}$$

where the five $\mathscr{W}$-operators are given in the Appendix. In the absence of bottom perturbations (i.e. $h = 0$), the wave perturbations, $o$ and $q$, decay to zero. We may see that these perturbations are enslaved to $h$ by considering the case where $h = 0$ (i.e. there are no bottom perturbations) and showing that, in this case, the wave-angle and amplitude perturbations are linearly decaying.

When $h = 0$ the equation for the wave-angle perturbation is

$$\frac{\partial o}{\partial t} = \mathscr{W}_{oo}o.$$

The first two terms of $\mathscr{W}_{oo}o$ are merely advection terms and the perturbation is assumed to be zero out to sea and bounded for all $y$. The third and fourth terms are the only ones that could cause instability. However, given our reference state, $\sin(\theta)$ and $\partial\theta/\partial x$ always have the same sign and $\partial H/\partial x$ is always positive so that wave-angle perturbations will always decay in the absence of bottom-topography perturbations.

As the wave-angle perturbations decay when $h = 0$, we need only consider

$$\frac{\partial q}{\partial t} = \mathscr{W}_{qq}q$$

when determining the stability of the wave amplitude in the absence of bottom-topography perturbations. Again, we will ignore the second term, which only represents advection in the $y$-direction. This leaves

$$\frac{\partial q}{\partial t} = \frac{\partial}{\partial x}\left[|\boldsymbol{C}_g|\cos(\theta)q\right] = -\frac{\partial}{\partial x}\left[C_g^x q\right].$$

We are interested in whether the perturbation $q$ grows or decays in time and thus will consider $q = \hat{q}e^{\lambda t}$, which gives

$$\lambda\hat{q} = -\frac{\partial}{\partial x}\left[C_g^x\hat{q}\right].$$

Taking $Q(x) = C_g^x\hat{q}$ this becomes

$$\frac{\partial Q}{\partial x} = -\lambda\frac{Q(x)}{C_g^x} = \lambda\frac{Q(x)}{\left|C_g^x\right|},$$

as $C_g^x < 0$. We may solve for $Q$, giving

$$Q(x) = Q(0)\exp\left(\int_0^x \frac{\lambda}{\left|C_g^x\right|}\,\mathrm{d}x\right).$$

However $\lim_{x\to\infty} Q = 0$ as $C_g^x$ is bounded at infinity and $\lim_{x\to\infty} q = 0$. This means that $\lambda$ must be negative and hence $q$ must decay with time.

Thus, in the absence of bottom perturbations the wave perturbations decay to zero. So all wave perturbations are enslaved to the bottom perturbations. Furthermore, the time scale for wave evolution is shorter than the time scale for the bottom topography. Thus, we assume that these adjustments are essentially instantaneous and solve for $o$ and $q$ as linear functions of $h$ by setting the left-hand side of (4.1) to zero.

The linearized equations of perturbations of the currents, sea elevation and bottom topography are

$$\left.\begin{aligned}
\frac{\partial u}{\partial t} &= \mathscr{M}_{uu}u + \mathscr{M}_{uv}v + \mathscr{M}_{uz}z + \mathscr{M}_{uh}h + \mathscr{M}_{uo}o + \mathscr{M}_{uq}q,\\
\frac{\partial v}{\partial t} &= \mathscr{M}_{vu}u + \mathscr{M}_{vv}v + \mathscr{M}_{vz}z + \mathscr{M}_{vh}h + \mathscr{M}_{vo}o + \mathscr{M}_{vq}q,\\
\frac{\partial z}{\partial t} - \frac{\partial h}{\partial t} &= \mathscr{M}_{zu}u + \mathscr{M}_{zv}v + \mathscr{M}_{zz}z + \mathscr{M}_{zh}h + \mathscr{M}_{zo}o + \mathscr{M}_{zq}q,\\
\frac{1}{\alpha}\frac{\partial h}{\partial t} &= \mathscr{M}_{hu}u + \mathscr{M}_{hv}v + \mathscr{M}_{hz}z + \mathscr{M}_{hh}h + \mathscr{M}_{ho}o + \mathscr{M}_{hq}q,
\end{aligned}\right\} \tag{4.2}$$

where the $\mathscr{M}$-operators are given in the Appendix. Equation (4.2) may be written in matrix form as

$$\boldsymbol{B}\frac{\partial}{\partial t}\boldsymbol{n} = \mathscr{M}\boldsymbol{n}, \tag{4.3}$$

where

$$\boldsymbol{B} = \begin{bmatrix} 1 & 0 & 0 & 0\\ 0 & 1 & 0 & 0\\ 0 & 0 & 1 & -1\\ 0 & 0 & 0 & \frac{1}{\alpha} \end{bmatrix}, \qquad \boldsymbol{n} = \begin{bmatrix} u\\ v\\ z\\ h \end{bmatrix}, \tag{4.4}$$

and $\mathscr{M}(x, \partial/\partial x, \partial/\partial y)$ is a differential operator in $x$ and $y$. The dependence on $o$, $q$ and $k$ is suppressed here because they can be represented as linear functions of $h$, as mentioned above.

In deriving the linearized bottom topography equation Calvete *et al.* (2002) ignored feedback terms from the topography to the wave orbital velocity (i.e. terms of the form $\partial u_w/\partial H$, $\partial u_w/\partial A$, and $\partial u_w/\partial k$). These feedback terms arise through the parameterization in terms of the orbital velocity in (2.5) and (2.6) and are given by (A 3) and (A 4). In order to compare the addition of the vortex force and Bernoulli

head terms to the model of Calvete *et al.* (2002) we also ignore these terms in most of the following. However, in § 5.4 we address how the results change by the inclusion of these terms.

If we assume

$$\boldsymbol{n}(x, y, t) = \hat{\boldsymbol{n}}(x, K_y)\mathrm{e}^{\lambda t + \mathrm{i}K_y y},$$

for $\lambda \in \mathbb{C}$, $K_y > 0$, then we may rewrite (4.3) as the eigenvalue problem

$$\boldsymbol{B}\lambda\hat{\boldsymbol{n}} = \mathscr{M}\left(x, \frac{\partial}{\partial x}, \mathrm{i}K_y\right)\hat{\boldsymbol{n}}, \tag{4.5}$$

with $K_y$ as a parameter.

We assume that the perturbations decay to zero for sufficiently large $x$ and use this condition in the eigenvalue problem (4.5). The boundary condition at the shore end for the velocity is the linearization of $U(0) = -U^{St}(0)$. For the bottom topography either Dirichlet, $h(0) = 0$, or Neumann, $\partial h/\partial x|_{x=0} = 0$, boundary conditions are prescribed. Dirichlet boundary conditions represent the situation where the bottom-topography perturbation is zero at the shoreward boundary. Neumann boundary conditions do not fix the perturbation at $x = 0$ but rather specify that the flux is zero at this boundary (it follows from setting $\boldsymbol{Q}\cdot\boldsymbol{n} = 0$ along with $U(0) + U^{St}(0) = 0$). Recalling that the water has depth $H_0$ at $x = 0$, we consider this the edge of the domain of interest and not the shoreline. This allows for the possibility that the perturbation may not disappear at this point. Previous studies have used the former of the above two boundary conditions and unless stated otherwise, so do we. We take the opportunity in this study to investigate how the results are affected by this alternative boundary condition as it is not obvious what physical mechanism would hold the perturbation at zero at the shoreward boundary.

We solve (4.5) for eigenvalues $\lambda(K_y)$, and eigenfunctions $\hat{\boldsymbol{n}}(x, K_y)$, using a rational Chebyshev method as described in Boyd (1987, 1989), Iranzo & Falques (1992) and Boyd, Rangan & Bucksbaum (2003). The equations are solved for 200 and 300 collocation points and the results compared to eliminate spurious eigenvalues as outlined in Boyd (1996). We use $L$ as the spacing parameter for the collocation points.

For a given $K_y$, an eigenfunction solution represents a mode with a periodicity $2\pi/K_y$ in $y$ with a growth rate given by the real part of $\lambda$, $\mathrm{Re}(\lambda)$. $\mathrm{Re}(\lambda)$ positive (negative) indicates a growing (decaying) solution. A positive (negative) imaginary part of $\lambda$, $\mathrm{Im}(\lambda)$, indicates that the mode advects in the negative (positive) $y$ direction with celerity $|\mathrm{Im}(\lambda)|/K_y$.

The ratio of the hydrodynamic time scale to the morphological time scale, $\alpha$, in $\boldsymbol{B}$ is small ($10^{-7}$ for the bed load and $10^{-5}$ for the suspended load morphological time scales). Previous studies have exploited this disparity in time scales to justify approximating $\boldsymbol{B}$ by

$$\boldsymbol{B} = \begin{bmatrix} 0 & 0 & 0 & 0 \\ 0 & 0 & 0 & 0 \\ 0 & 0 & 0 & 0 \\ 0 & 0 & 0 & 1 \end{bmatrix} \tag{4.6}$$

(note that there is a factor of $\alpha$ difference between these eigenvalues and those of the full problem). We call this the adiabatic approximation.

We know from Calvete *et al.* (2002) that for $\lim\alpha \to 0$ and with consideration of currents only (waves appearing only in parametric form) the solutions are morphologically similar to shore-connected ridges. Using the adiabatic approximation, the problem collapses to an eigenvalue problem in one variable, $h$. It implies that,

in the absence of changes in bottom topography, the flow is stable. As the bottom topography changes, the flow relaxes to a slightly perturbed flow to account for these changes. In the adiabatic approximation the eigenvalue problem represents a situation wherein this relaxation happens instantaneously when compared with the morphological time scale. However, if the equilibrium flow were to lose stability due to changes in the bottom topography this approximation would no longer be valid as the unstable eigenvalues associated with the flow would be suppressed by this simplification.

Furthermore, for some equilibrium flows and bottom topographies the adiabatic approximation may be appropriate, while for others it may not, i.e., setting $\alpha$ to zero is only justified if doing so does not artificially suppress instabilities. The consequences of these unstable degrees of freedom being significant might be, among other things, that the predicted shore-connected ridges are different from those observed in the physical setting. Restrepo (2001) attempted to settle this issue but this crucial aspect of the model remains open. Below we determine, for the particular equilibrium solution in question, whether waves are present or not, and how large $\alpha$ can be before the solutions deviate significantly from those obtained by Calvete *et al.* (2002).

### 4.2. *Questions of interest*

We will use the linear stability analysis to investigate the following questions:

*Waves versus no waves*

Using our equations, we investigate how the presence of waves affects the results obtained when currents alone compose the velocity field of the fluid. Note that we are only considering the conservative wave effects of the vortex force, Bernoulli head and Stokes drift (equivalent to the radiation stress terms). The model already includes parameterizations for the bottom friction and sediment transport that are based on the wave orbital velocity. We do not investigate changes to these parameterizations. When we refer to the no-wave case this still includes the bottom friction and sediment transport parameterizations as given by Calvete *et al.* (2002).

*Wave parameters* $\theta_\infty$, $|A|_\infty$, $\sigma$

We investigate how changes in the angle of incidence, amplitude and frequency of the waves are manifested in the topography of the erodible bed.

*Boundary conditions*

We investigate how the numerical calculation of the eigenfunctions depends on the choice of boundary condition on $h$ at $x = 0$. In particular, we compare setting $h$ to zero at $x = 0$ (Dirichlet), to setting $\mathrm{d}h/\mathrm{d}x$ to zero (Neumann). These represent no perturbation and no perturbation flux at the $x = 0$ boundary respectively. Following Calvete *et al.* (2002), our default boundary condition is the Dirichlet condition.

*Adiabatic assumption*

We determine a range of parameter values for which the adiabatic assumption is justified for the particular equilibrium solution that leads to shoreface-connected ridges and see how dropping this assumption changes the outcome of the linear stability analysis.

*Wave mechanisms*

We compare models with different levels of feedback to attempt to isolate the mechanisms by which the waves affect the outcome of the calculations. We also characterize the convergence/divergence of the waves and currents, a phenomenon that is instrumental in the evolution of the bottom topography and the formation of shoreface-connected ridge structures.

| Parameter | Value | Units | Description |
|---|---|---|---|
| $H_0$ | 14 | (m) | Depth at shore end |
| $H_\infty$ | 20 | (m) | Depth out to sea |
| $L$ | 5.5 | (km) | Horizontal length scale |
| $\beta$ | $1.1 \times 10^{-3}$ | (m/m) | Bottom slope $= (H_\infty - H_0)/L$ |
| $f$ | $9.3 \times 10^{-5}$ | (rad $s^{-1}$) | Coriolis parameter |
| $\nu_s$ | $1.0 \times 10^{-3}$ | $s^3\,m^{-3}$ | Coefficient, suspended-load transport |
| $\nu_b$ | $1.8 \times 10^{-4}$ | $s^2\,m^{-3}$ | Coefficient, bed-load transport |
| $\lambda_s$ | 2.5 | ($s^2\,m^{-1}$) | Smoothing, suspended load |
| $\lambda_b$ | 0.7 | | Smoothing, bed load |
| $s$ | $2 \times 10^{-7}$ | ($m\,m^{-1}$) | A longshore sea elevation slope |
| $\hat{r}$ | $2.4 \times 10^{-3}$ | | Bottom friction |
| $\tau_y$ | $-4.0 \times 10^{-4}$ | ($m^2\,s^{-2}$) | Kinetic surface stress |
| $\lvert A\rvert_\infty$ | 0.8 | (m) | Incoming wave amplitude |
| $\theta_\infty$ | | (rad) | Incoming angle of incidence |
| $\sigma$ | $\pi/5$ | (rad $s^{-1}$) | Frequency |

TABLE 1. Reference values for bottom topography, currents, and waves; values are consistent with those used in Calvete *et al.* (2002) with adjustments made because of the different parameterization of the wave orbital velocity. Unless otherwise stated these are the values that are used in the numerical calculations. Note that $\lambda_b$ and $\hat{r}$ are dimensionless parameters.

### 4.3. *Results and analysis*

We focus on the example of the ridges that form off Long Island, on the East Coast of the USA. When waves are suppressed the parameters are chosen to agree with those in Calvete *et al.* (2002). The agreement is not exact as they used a formula for wave orbital velocity based on bottom depth whereas we calculate it directly from the wave parameters according to (2.7). The general results, however, are still consistent with the Long Island setting with a longshore spacing of 4.3 km and an e-folding time of 125 years, giving a celerity of 1.9 m $yr^{-1}$ in the direction of the steady flow. While the effects of the waves alter these somewhat they are still within the range of reasonable solutions.

Unless otherwise stated, we assume the parameters are as given in table 1. Although the prevailing direction for the peak of the wave spectrum is around $\pi/18$ for Long Island we consider a range of incoming wave direction to explore the full range of possible effects of waves. Recall that $0 < \theta_\infty < \pi/2$ means that the waves come toward the shore from the north and east directions as depicted in figure 1. These waves are coming in in the same direction as the longshore current. For $-\pi/2 < \theta_\infty < 0$ the waves are coming in against the current (because we consider swell waves it need not be a contradiction to have waves coming in in the opposite direction to the prevailing wind).

Figure 2 shows the growth rate as solid lines plotted against the non-dimensionalized alongshore wavenumber of the instability $K_y L$, for various angles of incidence $\theta_\infty$. In all cases $|A|_\infty = 0.8$ m. For comparison, the growth rates for the 'no-waves' case are shown as dashed lines, superimposed on all the wave cases.

Waves coming in at steeper angles have a larger effect on the growth rates than waves close to normally incident. For $\theta_\infty = \pi/4$ the peak growth rate of the fastest growing mode is shifted to a lower alongshore wavenumber ($K_y$). The instabilities with higher alongshore wavenumber are suppressed to a greater extent and the relative position of the modes changes with the alongshore wavenumber. For waves that are

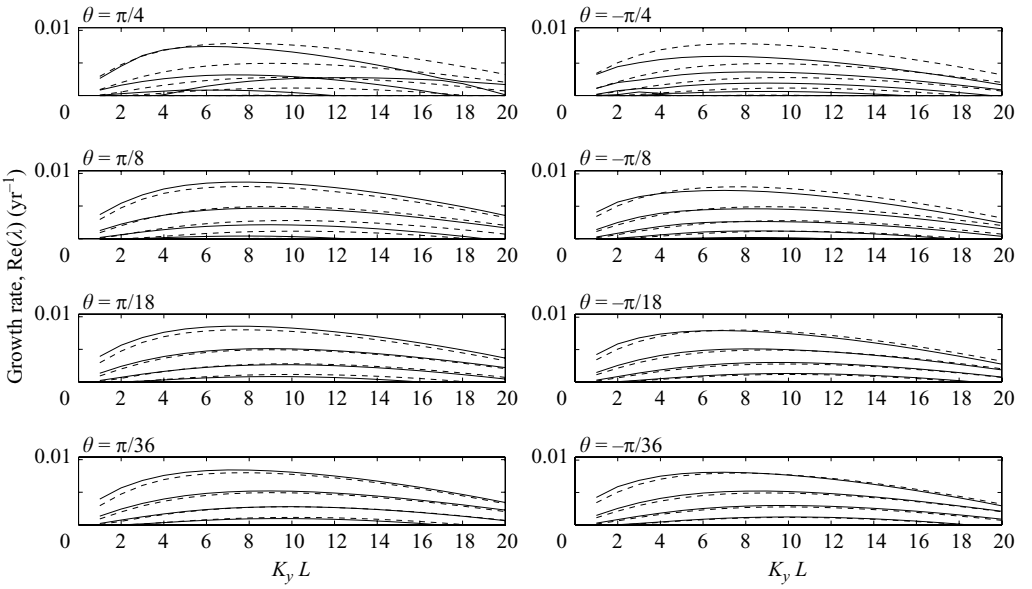


FIGURE 2. Growth rate ($yr^{-1}$) as a function of $K_y L$ for different angles of incidence of the waves. The dashed lines represent the outcome when the waves are suppressed. The waves have an incoming amplitude $|A|_\infty = 0.8$ m.

still coming in with the current but more normally to the shore there is less change in the growth rate. The growth rate of the fastest growing mode is slightly enhanced. Some of the more slowly growing modes have their growth rate suppressed. For waves coming in close to normal there is not much change in the growth rates, although the fifth unstable mode from the no-wave case is stable even for these values of $\theta_\infty$. For waves that come in at a steep angle from normal, against the current, the growth rate is suppressed and the fastest growing mode is shifted to lower alongshore wavenumber.

Figure 3 shows the first three unstable modes for the no-wave case (first column) and the wave cases for different values of $\theta_\infty$ for alongshore wavenumber of $K_y L = 8$ (which has the peak growth rate for the no-wave case). The most striking feature of the unstable modes for waves with $\theta_\infty$ positive is the number of modes that are long narrow features forming at an acute angle with the shoreline, very similar to shoreface-connected ridges. Without the waves, the first mode has this feature but all the subsequent modes are patchy with the second mode having two layers of patches, the third, three and so on (see the first column of figure 3). For waves coming in against the current but close to normally incident the patchy modes are stretched out similarly to the case with $\theta_\infty$ positive. For $\theta_\infty < 0$ and coming in at a steeper angle with the shore they are closer to the patchy modes of the no-wave case. For $\theta_\infty = -\pi/18$ the modes are transitional between patchy and stretched out, while for $\theta_\infty = -\pi/4$ the modes can be seen to be similar to the no-waves case.

Thus for $\theta_\infty = \pi/18$ (the peak wave direction for Long Island), the modes form long thin ridges at a steep angle with the shore. Thus, the waves significantly alter the unstable modes with smaller growth rates. The waves have less effect on the first unstable mode, which always was linear, up-current-rotated ridges. Nonlinear modelling of the sediment problem in Calvete *et al.* (1999), however, suggests that the lesser unstable modes may also be important in explaining the final bottom

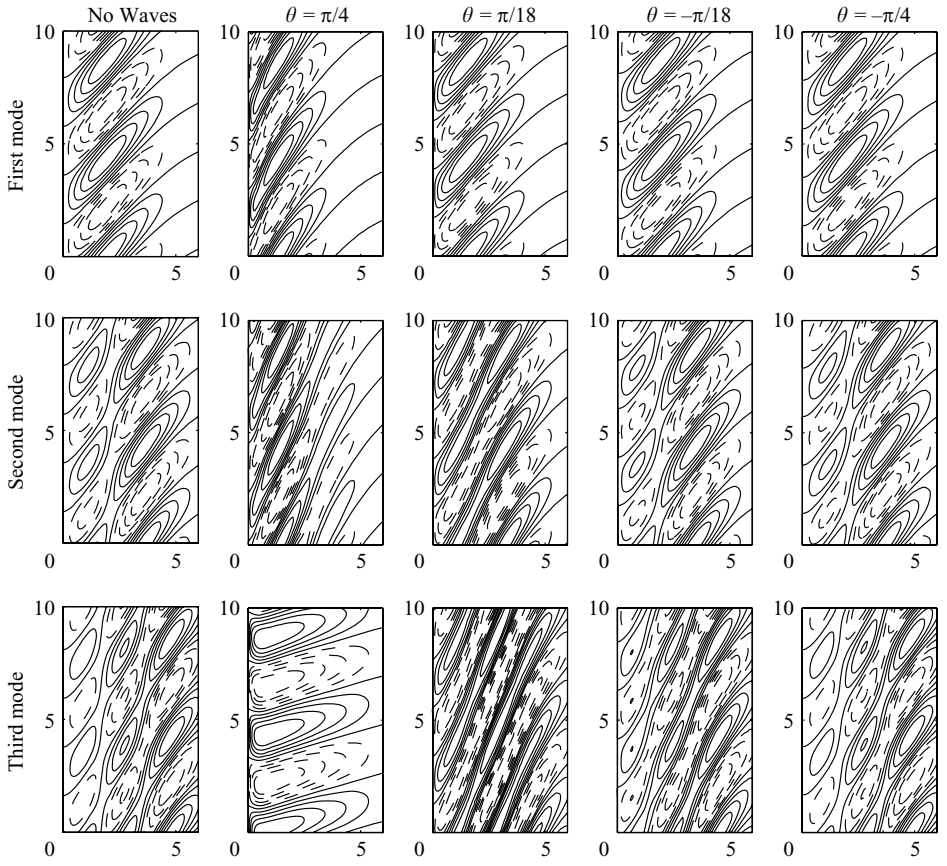


FIGURE 3. Largest three unstable modes for peak growth rate for the no-wave case and also for waves with angle of incidence $\theta_\infty = \pi/4$, $\pi/18$, $-\pi/18$ and $-\pi/4$. For $\theta_\infty = \pi/4$, the third mode is a wave-induced mode that is stable when wave effects are not included. Incoming wave amplitude is $|A|_\infty = 0.8$ m. The shoreward end is the left side of the rectangles. The axes have dimensions of km. Dashed lines represent negative contours.

topography after the instability has saturated. Thus, this change in the shape of the mode due to waves may enhance the formation of shoreface-connected ridges.

Waves with positive $\theta_\infty$ also push the unstable modes further onshore so that there is a steeper drop-off to zero at $x = 0$ and the modes do not extend as far offshore. For large positive values of $\theta_\infty$ (shown for $\theta_\infty = \pi/4$ in figure 3) there is a very different mode: the third most unstable mode. It is slightly up-current rotated but much closer to normal to the shoreline than any of the other modes. We call this the wave-induced mode. For smaller values of $\theta_\infty$ this mode becomes stable.

Figure 4 shows the effect of the waves on the celerity of the fastest growing mode as a function of $K_y L$. The waves tend to increase the celerity when they are coming in the same direction as the current (i.e. $\theta_\infty > 0$). Waves coming in at a steep angle can alter the celerity by several metres per year. For $\theta_\infty < 0$ the effect is not as strong; in this case figure 4 shows the celerity being increased for low alongshore wavenumber and very slightly decreased for higher alongshore wavenumber. As observed in Calvete *et al.* (2002), the suspended-load term of the sediment transport basically drives the instability whereas the bed-load term ensures that it has the correct celerity. Based on

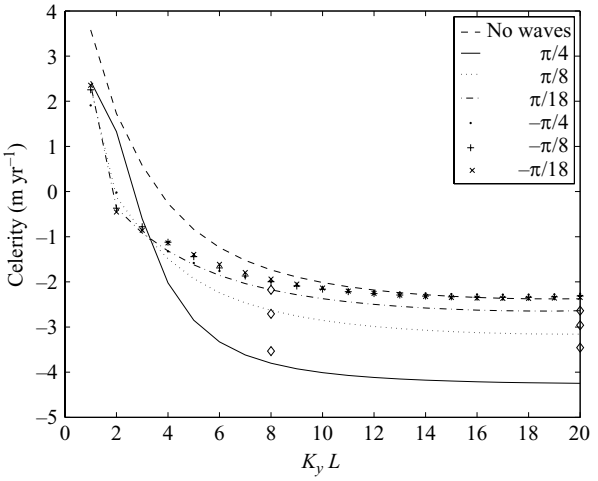


FIGURE 4. Celerity (m yr$^{-1}$) of fastest growing mode for waves with an angle of incidence of $\theta_\infty = \pm\pi/4, \pm\pi/8, \pm\pi/18$. (Positive values make the instability travel faster in the downstream direction.) Diamonds indicate what the celerity would be if it were strictly proportional to the Stokes drift for positive angles of incidence.

this we look at how the waves affect the two components of the sediment transport separately to understand their overall effect on the equations. For the suspended load only, the celerity of the instabilities is actually oppositely signed, i.e. the ridges travel upstream, in the opposite direction to the current. When waves travelling in the same direction as the current are included in the model the celerity becomes negative so that the instability moves in the same direction as the current. For waves coming in at $\theta_\infty = \pi/4$, the celerity is of the order of 2 m yr$^{-1}$, in line with the observed ridge celerity. For waves coming in nearly perpendicular to the shore the effect is not as strong, however. This makes sense in terms of the suspended sediment being advected by the Stokes drift in addition to the current. However when the waves are against the current, i.e. $\theta_\infty < 0$, the effect is far weaker, i.e. the sediment is not slowed by a similar amount to that which it is enhanced by waves and currents acting in unison. The effect of the waves on the bed load is primarily related to the angle of the waves. Waves that come in at a steep angle slow the advection of the instability irrespective of whether they are with or against the current. Waves that come nearly perpendicular to the shore have a smaller effect. There is a secondary effect due to the longshore Stokes drift. The overall celerity of the full model can be seen as a combination of these two effects. The changes in the celerity for $\theta_\infty < 0$ are less pronounced than the changes for $\theta_\infty > 0$. For $\theta_\infty > 0$ the celerity is always enhanced by an amount roughly proportional to the longshore Stokes drift; whereas for $\theta_\infty < 0$ the celerity is sometimes slowed and in other instances enhanced.

When the waves are very small (say $|A|_\infty = 0.1$ m and below) they have little effect on the outcome, compared to the no-wave case (recall that the no-wave case still includes the full effects of the wave orbital velocity on bottom friction and sediment transport). For $\theta_\infty = \pi/18$ there is only a small difference between the growth rates with and without waves (see figure 2). As $|A|_\infty$ increases the growth rate shifts from the no-wave case to the wave case. The two fastest growing modes are slightly enhanced and the other modes are slightly suppressed; the fifth unstable mode is suppressed.

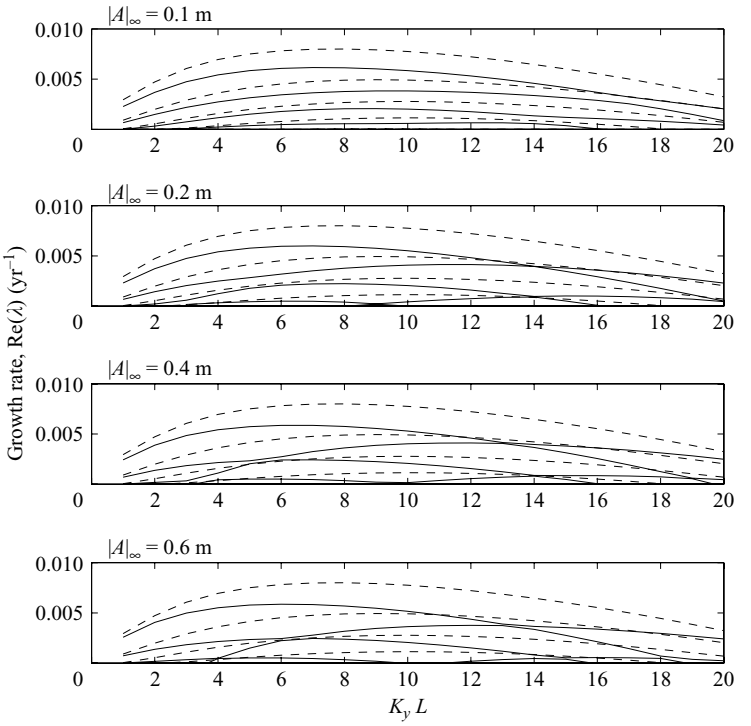


FIGURE 5. Growth rate (yr$^{-1}$) as a function of $K_y L$ and incoming amplitude of the waves $|A|_\infty$. The dashed lines represent the instabilities due to currents alone. The angle of incidence of the waves is fixed at $\theta_\infty = \pi/4$.

For other (albeit less realistic) values of $\theta_\infty$ there are more noticeable changes. Figure 5 shows how the amplitude of the waves affects the growth rate of the instability for waves coming in at an angle of $\theta_\infty = \pi/4$. As the height of the incoming waves increases some of the modes are suppressed at higher longshore wavenumbers while others are enhanced. The peak growth rate moves towards smaller longshore wavenumbers and for $|A|_\infty = 0.6$ m it is for longshore wavenumber of around $K_y = 6/L$.

As the wave amplitude increases, say $|A|_\infty = 1.5$ m, the waves tend to smooth modes with higher alongshore wavenumbers while increasing the growth rate of those modes which remain unstable. The most unstable mode is shifted to lower alongshore wavenumbers and the higher alongshore wavenumber instabilities are suppressed. Note that for $|A|_\infty = 1.5$ m, the wave slope $\epsilon = k|A|$ is around 0.1 and thus the wave equations derived in MRL04 remain valid.

For increasing values of the incoming wave amplitude the modes shift from the no-wave modes (where the second, third, fourth and fifth modes are 'patchy' – see the first column of figure 3) to the modes with waves (the remaining columns of figure 3). For waves coming in close to perpendicular to the shore this means that the patchy modes stretch out and align to form the long thin up-current-rotated modes. Thus all the unstable modes are up-current-rotated ridges in this case. For $\theta_\infty = \pi/4$ the wave-induced mode becomes unstable for larger values $|A|_\infty$ and increases in prominence.

In the numerical calculations reported here we set the wave period to 10 s but periods of 7, 15 and 20 s were also considered. There is little qualitative change in the linear stability analysis for period variations within this range. Interestingly, the

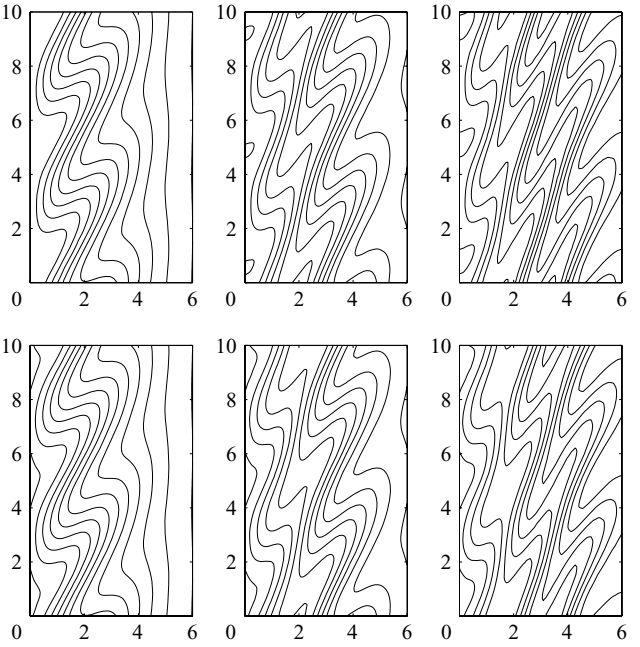

FIGURE 6. Reference and perturbation bottom topography for the three fastest growing modes for Dirichlet (top) and Neumann (bottom) boundary conditions on $h$ at $x = 0$. $\theta_\infty = \frac{\pi}{18}$, $|A|_\infty = 0.8\,\mathrm{m}$ and $K_y L = 8$.

amplitude of the waves with a period of 7 s decreases as the waves come inshore at this depth while for periods of 10 s and above the waves are shoaling and so their amplitude increases. This does not appreciably affect the solutions, though, because the wave orbital velocity and Stokes drift still increase with decreasing depth due to the changes in the other parameters. The wave-induced mode is slightly more prominent for a period of 7 s and the effect on the celerity is closer to being purely that of advection by the Stokes drift. These are all fairly small changes however.

Changing the boundary condition for $h$ at $x = 0$ from Dirichlet to Neumann affects the morphology of the instabilities close to the shoreline. The growth rate of the stability is not strongly affected, nor is the celerity. Figure 6 shows the first three unstable modes for both Dirichlet and Neumann boundary conditions. The reference bottom topography is shown in addition to the perturbation, giving an idea what a bathymetric map of how these perturbations would look. For the Dirichlet boundary conditions the modes sometimes have a small boundary layer near $x = 0$ where they dip down to zero at $x = 0$. Because this is not fixed in the case of the Neumann boundary conditions there are still small longshore oscillations in the modes at $x = 0$. This difference is most obvious for the cases with waves coming in with the currents ($\theta_\infty > 0$) as the modes are pushed up against the shoreline. Apart from this alteration near the shoreline, the gross features of the instabilities remain unchanged. The robustness of the solutions to the different boundary conditions suggests that the eigenfunctions are a genereal feature of the system and not strongly tied to details in the boundary set-up.

To test the adiabatic approximation we considered the full problem using $\boldsymbol{B}$ as given by (4.4) rather than by (4.6). The results from the full problem were not significantly different from the reduced problem, which confirms that the adiabatic approximation

is a reasonable assumption. For $\alpha$ up to around unity similar results were obtained. When $\alpha$ was larger than this the unstable growth rate began to decrease and the wave effect became less pronounced but the up-current-rotated bars were still unstable. This suggests that even if the morphological time scale were similar to the hydrodynamic time scale instabilities in the bed-form like those shown here would still occur. Furthermore, when the bottom topography is held constant (i.e. $h = 0$), the current solution is found to be linearly stable. Thus, the current perturbations are enslaved to the bottom topography. The addition of waves does not change this stability.

## 5. Wave effects

In order to better understand the effect that waves have on the bottom topography we ran several experiments:

(i) No forced current. We consider the effect of the waves when the wind stress and pressure gradient are both set to zero.

(ii) Wave pathways. We investigate the different pathways by which the waves affect the erodible bed.

(iii) Convergence. We look at the convergence patterns of the waves and currents and correlate them with the bottom topography patterns.

(iv) Feedback of wave orbital velocity. We consider how the instability is affected if the feedback of the wave orbital velocity is included.

### 5.1. *No forced current*

We consider what happens when the wind stress $\boldsymbol{\tau}$ and pressure gradient $s$ are both set to zero. Without the waves the current is zero. The addition of the waves drives a cross-shore flow that balances the cross-shore Stokes drift. The longshore flow is zero. The only net movement of particles is in the longshore direction due to the longshore Stokes drift.

Both of these cases (with and without waves) are linearly stable, with the real parts of all the eigenvalues negative for all wavenumbers and modes. The addition of the waves does not significantly alter this, although it does change the decay rates and adds a longshore migratory component to the decay.

The fact that the waves by themselves only smooth the bottom topography suggests that the wave-induced instability that occurs for $\theta_\infty$ large and positive (see figure 3) is not simply a wave instability but must also be due to some interaction with the currents.

### 5.2. *Wave pathways*

As illustrated in figure 7, there are three pathways by which the conservative waves effects can change the evolution of the erodible bed. These are:

(1) The original addition of the equilibrium wave solution to the current and its effect on the perturbations of the current and the bottom topography. We refer to this as the primary wave effect.

(2) The perturbation of the bottom topography affects the waves. This can cause convergences of the Stokes drift, which in turn affects the bottom topography. We call this the direct wave feedback.

(3) The wave perturbation also feeds back into the bottom topography indirectly. The wave perturbation alters the current perturbation, which in turn alters the bottom topography perturbation. We call this the indirect wave feedback.

In order to understand the effects of these three pathways, we ran three numerical experiments where we shut off different pathways. In the first experiment we keep the

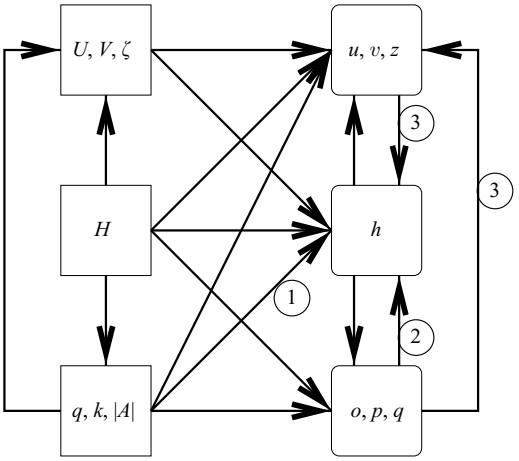


FIGURE 7. Schematic diagram of how variables influence each other. (1), (2) and (3) are the three pathways by which the waves influence the erodible bottom corresponding to those described in the text.

primary wave effect but assume that there is no feedback from the bottom topography to the waves, i.e. we retain pathway (1) but remove pathways (2) and (3). The second experiment allows feedback from the erodible bed to the waves and back, but only directly, via the convergence of the Stokes drift, i.e. we keep pathways (1) and (2) but remove pathway (3). The only feedback in the third experiment is indirect, via the current perturbations, i.e. we keep pathways (1) and (3) but remove pathway (2). Note that, because it does not make sense to have a wave perturbation without first having a wave, we do not consider cases where we have wave feedback (pathways (2) and (3)) without having the primary wave effect (pathway (1)).

When only pathway (1) is incorporated into the model the growth rates of the unstable modes are decreased. As in the full case the strongest effect is seen for waves coming in at steep angles but with only pathway (1) the suppression is seen for all waves angles whereas when the other feedbacks are incorporated the growth rates of some of the modes are enhanced by the waves (especially waves coming in closer to normal but with the current). The shapes of the unstable modes, however, are almost exactly the same as without the waves in this case and there is no wave-induced mode for any values of $\theta_\infty$. The celerity is slowed slightly for waves coming in at a steep angle (positive or negative) but there is very little change for waves coming in closer to perpendicular to the shore.

When the primary wave effect and one or the other feedback are incorporated into the model it is not as stable as when both the feedbacks are included or neither of them. With pathways (1) and (2) the growth rates are similar to those observed for the full wave model; however some of the higher frequencies have large growth rates but these may just be spurious. The unstable modes in this case are similar to the stretched modes seen in the full case and the wave-induced mode is seen for large positive values of $\theta_\infty$. If anything the second and third modes are slightly more stretched out than in the full model, especially for waves with $\theta_\infty$ negative. The celerity is increased slightly for all values of $\theta_\infty$. For pathways (1) and (3) the growth rates are again not affected much except for large values of $\theta_\infty$ where they are somewhat suppressed. The modes are also little changed from the no-wave case although for $\theta_\infty$

positive they are very slightly more stretched out. There is no wave-induced mode. The celerity is decreased slightly for all values of $\theta_\infty$.

Thus, most of the effects of the waves are caused by the direct feedback of the waves into the bottom topography equation (i.e. recognizing that tracers are advected by the Lagrangian current rather than the Eulerian current). The primary wave effect alters the growth rate of the instabilities somewhat but does not affect the shape of the modes nor does it induce any new instabilities. The indirect feedback has little effect in itself but does stabilize the problem and give better numerical solutions when it is included. The celerity seems to be affected differently by the different features of the waves. The full effect of the waves on the celerity seems to be a blend of these differing effects.

### 5.3. *Convergence*

The bottom-topography evolution equation has two components: a convergence term and a diffusion term. The diffusion term represents smoothing of the bottom. Moreover, it is physically significant as it sets a length scale for the ridges. Instabilities occur due to the convergence term which is related to the convergence of the current (and Stokes drift) but modified by the wave orbital velocity, i.e. $-\nabla_\perp\cdot(c_b|u_w|^2 + c_s|u_w|^3H)(\boldsymbol{V}+\boldsymbol{V}^{St})$, where $c_b = \nu_b H_0/U_{w0}^2$ and $c_s = \nu_s/U_{w0}^3$ (Our model differs from that of Calvete *et al.* (2002) in that the convergence term includes both the current and the Stokes drift). In order to understand the way that the waves change the shapes of the existing modes and enhance the wave-induced mode we look at these convergences, both of the current and Stokes drift and of the sediment transport related to these quantities. In the linear stability analysis the sediment transport convergence becomes

$$\frac{\partial}{\partial x}[-K(x)(u+\mathrm{d}U^{St})] + \frac{\partial}{\partial y}[-K(x)(v+\mathrm{d}V^{St}) + c_s|u_w|^3(V+V^{St})h],$$

where

$$K(x) = c_b|u_w|^2 + c_s|u_w|^3H,$$

and we assume that the wave components are enslaved to $h$, i.e. $\mathrm{d}\boldsymbol{V}^{St} = (\mathrm{d}\boldsymbol{V}^{St}/\mathrm{d}h)h$, where

$$\frac{\mathrm{d}\boldsymbol{V}^{St}}{\mathrm{d}h} = \frac{\partial \boldsymbol{V}^{St}}{\partial k}\frac{\partial k}{\partial h} + \frac{\partial \boldsymbol{V}^{St}}{\partial \theta}\frac{\partial \theta}{\partial h} + \frac{\partial \boldsymbol{V}^{St}}{\partial |A|^2}\frac{\partial |A|^2}{\partial h} - \frac{\partial \boldsymbol{V}^{St}}{\partial H}.$$

Note that, as discussed in § 4.1, it is also possible to include the feedback of the bottom topography on the wave orbital velocity by including the $\partial|u_w|/\partial h$ terms given at the end of the Appendix. The addition of these terms is discussed in § 5.4.

The expressions for the Stokes drift perturbation with respect to changes in the wave quantities and the depth are

$$\frac{\partial \boldsymbol{V}^{St}}{\partial k} = -\frac{g|A|^2}{2\sigma}\begin{pmatrix}\cos\theta\\ \sin\theta\end{pmatrix}, \qquad \frac{\partial \boldsymbol{V}^{St}}{\partial \theta} = \frac{g|A|^2k}{2\sigma}\begin{pmatrix}\sin\theta\\ -\cos\theta\end{pmatrix},$$
$$\frac{\partial \boldsymbol{V}^{St}}{\partial |A|^2} = -\frac{gk}{2\sigma}\begin{pmatrix}\cos\theta\\ \sin\theta\end{pmatrix}, \qquad \frac{\partial \boldsymbol{V}^{St}}{\partial H} = \frac{g|A|^2k}{2\sigma H^2}\begin{pmatrix}\cos\theta\\ \sin\theta\end{pmatrix}.$$

The wavenumber is affected by perturbations in the bottom topography according to

$$\frac{\partial k}{\partial h} = -\frac{\partial k}{\partial H} = \frac{2k^2}{\sinh(2kH)+2kH}.$$

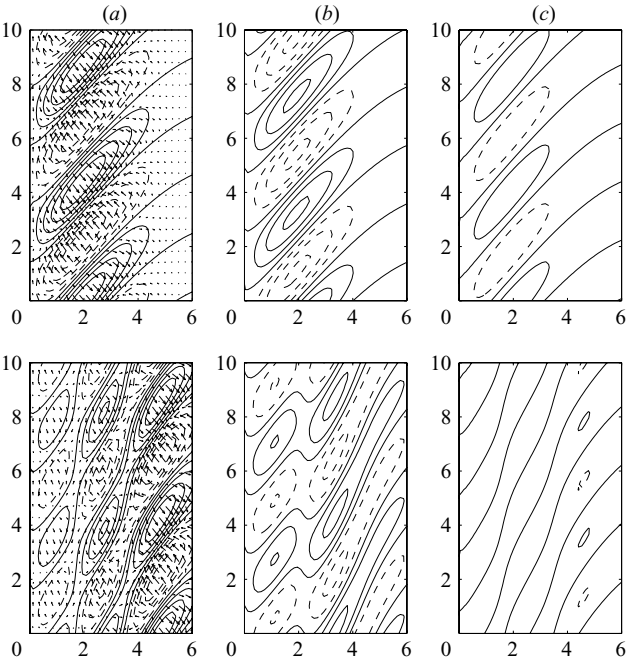


FIGURE 8. No-waves case, $K_y L = 8$. Top: first mode, bottom: third mode. (*a*) Contours show bottom topography perturbation (dashed lines negative) and arrows show current perturbations. (*b*) Convergence of current perturbations ($\nabla \cdot \boldsymbol{u}$). (*c*) Convergence of sediment transport perturbations ($\nabla \cdot K(\boldsymbol{x})\boldsymbol{u}$) (solid lines indicate convergence, dashed lines divergence).

Likewise for $\theta$ and $|A|^2$,

$$\frac{\partial \theta}{\partial h} = -\mathscr{W}_{oo}^{-1}\mathscr{W}_{oh},$$

$$\frac{\partial |A|^2}{\partial h} = -\mathscr{W}_{qq}^{-1}\left[\mathscr{W}_{qh} - \mathscr{W}_{qo}\left(\mathscr{W}_{oo}^{-1}\mathscr{W}_{oh}\right)\right],$$

where the $\mathscr{W}$ operators are given in the Appendix. These last two partial derivatives are notable in that they depend upon differential operators and their inverses and must be evaluated numerically.

In the no-waves case, the plot of the current convergence looks similar to the bottom topography, save for a phase shift (see figure 8). The flow diagram shows the currents being deflected offshore over the ridge crests. As mentioned by Trowbridge (1995) and Falques *et al.* (1998*b*), the offshore deflection is balanced by a convergence of flow. The maximum current convergence happens approximately a quarter of a period downstream from the ridge crest. The sediment transport is linearly related to the current with a coefficient that is a function of the wave orbital velocity. Convergence of the sediment transport occurs closer to the crest than that of the current (see figure 8*b*, *c*) but still slightly downstream. This causes the ridge to grow beyond its crest, i.e. the flow scours sand from the upstream side of the ridges and deposits it on the downstream side. Thus the ridges are advected downstream as they develop. For the patchy modes the current is also pushed offshore over the humps and shoreward over the depressions. The current convergence over the shorewardmost bump is further downstream than over the outer bumps. Again the sediment transport

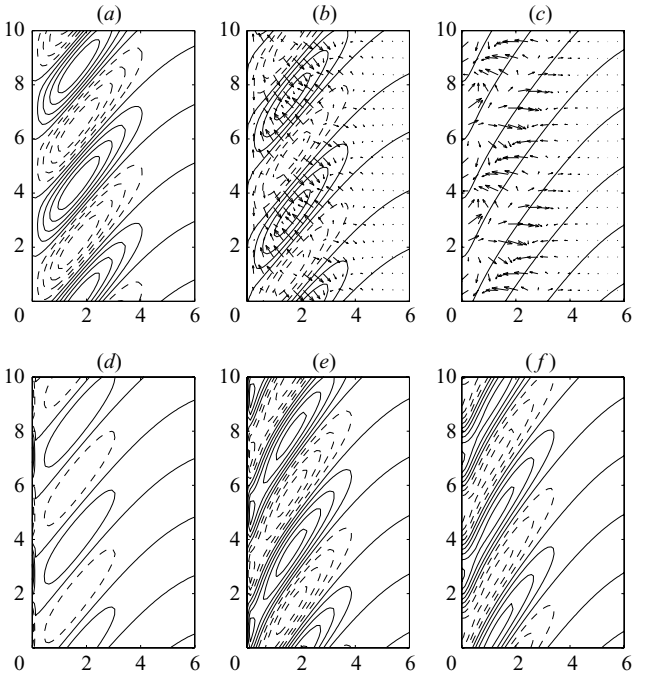


FIGURE 9. First mode, $\theta_\infty = \pi/18$, $|A|_\infty = 0.8\,\mathrm{m}$, $K_y L = 8$. (*a*) Bottom topography perturbation (dashed lines negative). (*b*) Current convergence (contours) and current perturbations (arrows). (*c*) Stokes drift convergence (contours) and Stokes drift perturbations (arrows). (*d*) Total sediment transport convergence. (*e*) Sediment transport convergence due to current. (*f*) Sediment transport convergence due to Stokes drift (solid lines indicate convergence, dashed lines divergence).

convergence is closer to the humps than the current convergence but still downstream of the crests.

When the waves are added both the current and the Stokes drift need to be considered (see figures 9 and 10 for the current and Stokes drift perturbation and corresponding sediment transport convergence). For the ridge-like modes (the original first mode and the long thin modes that form from the patchy modes in the presence of waves with positive angle of incidence), the situation for the currents is still very similar to no-waves case, i.e. the current is pushed offshore over the ridges and the maximum convergence occurs approximately a quarter of a period downstream of the crest of the ridge. The Stokes drift perturbation is most prominent near the shore. The Stokes drift is deflected shoreward over the ridges towards the upstream side, and is enhanced (flowing shoreward) over the top of the ridge and just upstream of the ridge at the shoreward edge of the domain. Where the ridge begins at the shoreward side the Stokes drift is decreased through sheltering, which causes convergence.

The convergence of the Stokes drift is five to ten times smaller than that of the currents (note that the Stokes drift itself is a factor of ten smaller than the alongshore current when $|A|_\infty = 0.8$ m). However, the sediment transport convergence due to the current and the Stokes drift are comparable in size but out of phase; the sediment transport due to currents being about a quarter phase downstream of the ridges whereas the sediment transport convergence due to the Stokes drift has a maximum slightly upstream of the ridge crest. The total convergence is thus smaller (on the same

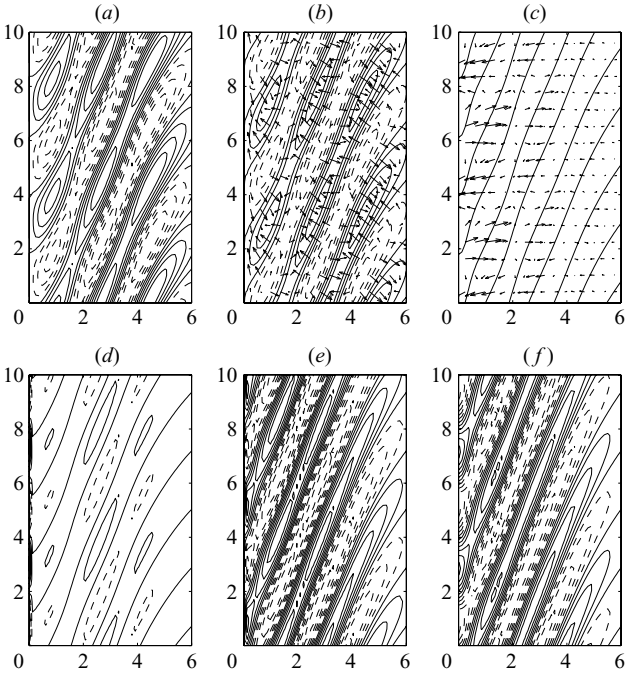


FIGURE 10. As figure 9 but for third mode.

order as the no-wave case). It is positioned with its maximum slightly downstream of the ridge crest. (Note that the contour scale for the convergence is the same for figures 8, 9 and 10 for ease of comparison.) Thus, although the Stokes drift is considerably smaller than the current it is just as important in forming the stretched out up-current-rotated ridges. The incoming waves tend to align the 'patchy' modes into long thin up-current-rotated ridges. There is also considerable sediment transport convergence near the shore which explains why the ridges are pushed closer up against the shore with the inclusion of the waves.

### 5.4. *Inclusion of wave orbital velocity feedback terms*

As mentioned in § 4, the feedbacks that we have included here are simply those that affect the conservative wave effects (i.e. the vortex force and the Bernoulli head). The model also includes non-conservative wave effects through the bottom friction and sediment flux parameterizations based on the wave orbital velocity (Calvete *et al.* 2002). Changes in the bottom topography would also affect the wave orbital velocity and thus would feed back into the equations through these parameterizations. Following Calvete *et al.* (2002), these feedback terms in the linearization of the bottom topography evolution equation and bottom friction were ignored (i.e. (4.2) with coefficients given by (A 2) were used omitting the terms (A 3) and (A 4)). These terms are proportional to derivatives of $u_w$ with respect to $H$, $A$, and $k$. In the case of Calvete *et al.* (2001*b*, 2002) they are equivalent to the derivative of $u_w$ with respect to $H$ in their linearized bottom evolution equation and bottom friction term, and hence, the outcomes that are discussed in what follows apply to them as well. A natural question to ask is what happens when the terms are retained: are the results so far discussed still valid?

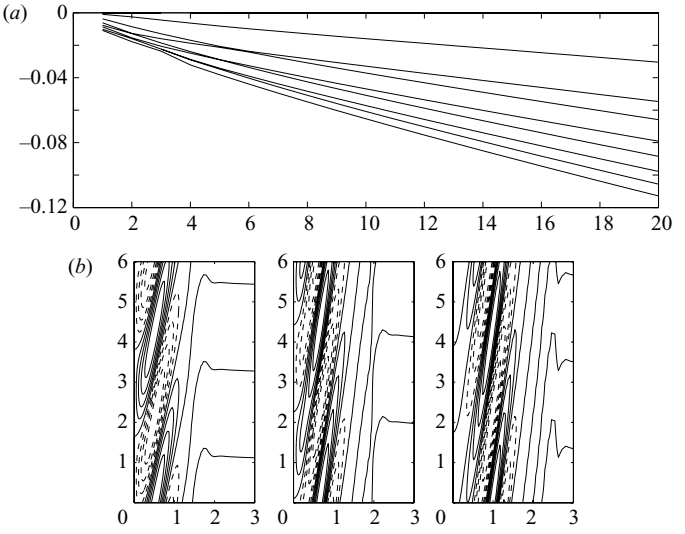


FIGURE 11. (*a*) Growth Rate ($yr^{-1}$) as a function of $K_y L$ for a case with feedback to wave orbital velocity included. (*b*) First three modes for $K_y L = 8$. This is the no-wave case; however the wave orbital velocity has $|A|_\infty = 0.8$ and period of 10 s.

While the feedback into the bottom friction does not significantly affect the model, the feedback into the bottom topography equation does, as shown in figure 11. The parameters are the same as in figure 8. With the inclusion of these terms all the instabilities are suppressed and the reference bottom is unchanged. The term proportional to derivative of $u_w$ with respect to $H$ (and thus $\theta$, $k$ and $|A|^2$) overwhelms the other convergence terms that were causing the instability. This general result also holds for Calvete *et al.* (2001*b*) and Calvete *et al.* (2002).

The consequences of this outcome are that the parameterization of the fluxes in terms of the wave orbital velocity is not correct, and that the model does not predict shore-connected ridges for parameter values reflecting the oceanic setting. The way the parameterization is made, however, appeals to common sense rather than physics, and thus we would suggest that the model should not be discounted, but rather, that the parameterization should be revisited.

## 6. Conclusions

This analysis shows that waves have a significant effect on the instability of the bottom topography. The main effects are:

(i) The waves alter the shape of the unstable modes. For waves coming in nearly perpendicular to the flow or with the flow, the patchy modes are stretched out into long thin modes. The Stokes drift advects sand inwards forming the patches into ridges. The mechanism behind this change seems to mainly involve the feedback of the waves into the bottom topography. The indirect feedback through the currents plays a lesser role. For $\theta_\infty > 0$ the waves also push the instabilities onshore. Although the Stokes drift is considerably smaller than the current it plays a crucial role in the divergence of the sediment transport term.

(ii) The waves change the celerity of the instability (i.e. affect $\mathrm{Im}(\lambda)$). This appears to be related to the advection as (at least for $\theta_\infty > 0$, i.e. the waves and current travelling in the same direction) the affect on the celerity is nearly proportional to

the alongshore Stokes drift. For $\theta_\infty < 0$ (i.e. the wave coming in against the currents) this effect is less clear.

(iii) The waves may suppress or augment the instability, i.e. affect $\mathrm{Re}(\lambda)$, the growth rate of the instability. They may also push the peak growth rate to longer alongshore instabilities. This affect is small for moderate waves with angles of incidence close to perpendicular to the shore.

(iv) For $\theta_\infty$ large and positive (i.e. around $\pi/4$), the waves excite a completely different instability and thus lead to morphology changes. This mode seems to be related to the direct wave feedback into the bottom topography.

(v) Increasing $|A|_\infty$ simply causes shifts between the no-wave case and the wave case. The changes are different depending on the incoming wave angle, $\theta_\infty$.

(vi) The frequency $\sigma$ (and hence also $k$) does not significantly affect the erodible bed.

(vii) The choice of boundary condition for $h$ at the shoreward end does not significantly affect the morphology of the instabilities. The features of the eigenfunctions are altered slightly close to the onshore edge to accommodate the specific boundary conditions. The Neumann boundary conditions follow from the assumption that $\boldsymbol{Q}\cdot\boldsymbol{n} = 0$ at $x = 0$ along with $U(0) + U^{St}(0) = 0$. This condition, that the shore-normal sediment transport is zero at the shoreward edge, is easier to imagine than the situation where the bottom perturbation is held at a fixed value (i.e. zero).

(viii) The adiabatic approximation is valid for the equilibrium solution studied here: in fact even for values of $\alpha$ around 1 the solutions do not differ much which suggests that these results may hold even if the morphological time scale is similar to the hydrodynamic time scale. However, our analysis can only confirm this finding for the particular equilibrium solution under consideration.

The addition of waves to the hydrodynamics significantly changes the bed-form instability through altering the shape and celerity of the unstable modes, suppressing or enhancing growth rates and in some cases introducing new unstable modes. These changes are predominantly driven by the vortex force and Stokes advection. The Bernoulli head plays a lesser role. How the instability is affected depends upon the wave parameters, most significantly incoming-wave angle and wave height. These differences may help explain why shoreface-connected ridges occur in some areas and not others.

This paper assumes steady monochromatic unidirectional waves which is not generally the case, especially in storm conditions. We are able to show, however, that the effect of waves cannot be ignored.

Inclusion of the feedback to the wave orbital velocity suggests that there are problems with this, at least in the parameterization of the sediment flux. If this model is to continue to be used to explain the formation of shore-connected bars this issue will need to be resolved.

There is general consensus that the ridges are greatly affected by storm-driven flows. This scenario cannot be convincingly explored using a current-only hydrodynamic model (the analysis in MRL04 suggests that wave effects cannot be merely parametrized). Furthermore, there is no way to gauge how specialized the results from a particular (though physically reasonable) equilibrium solution carry over to the more general case, in which a hydrodynamic and sediment dynamic model would evolve using temporal climatology. An analysis of the results from an evolutionary model with forced climatology would be a logical next step. Future work will look at the questions of unsteady forcing and more general wave climates.

The authors are grateful to Jim McWilliams and Mac Hyman for the many stimulating discussions. This work was performed while the J. M. R. was a summer visitor of the T7 Division at Los Alamos National Laboratory. This work was made possible by NSF Grant DMS-327617 and DOE Grant DE-FG02-02ER25533. E. M. L. also acknowledges the help of the University of Canterbury Mathematics Department and National Institute of Water and Atmospheric Research (NIWA) New Zealand. We also appreciate the work of the anonymous referees whose comments have made this paper much stronger.

## Appendix. Terms in linear stability calculations

Here we give the coefficients for equations (4.1) and (4.2). The coefficients for the wave equations (4.1) are

$$\mathscr{W}_{oo}o = |C_g|\left(\cos(\theta)\frac{\partial o}{\partial x} + \sin(\theta)\frac{\partial o}{\partial y}\right) - \left(|C_g|\sin(\theta)\frac{\partial \theta}{\partial x} + \frac{\sigma\cos(\theta)}{\sinh(2kH)}\frac{\partial H}{\partial x}\right)o, \tag{A 1a}$$

$$\mathscr{W}_{oh}h = \left(-\left(\frac{\partial|C_g|}{\partial k}\frac{\partial k}{\partial H} + \frac{\partial|C_g|}{\partial H}\right)\cos(\theta)\frac{\partial\theta}{\partial x} - \frac{2((\partial k/\partial H)H + k)\sigma\cosh(2kH)\sin(\theta)}{\sinh^2(2kH)}\frac{\partial H}{\partial x} - \frac{\sigma\cos(\theta)}{\sinh(2kH)}\frac{\partial}{\partial y} + \frac{\sigma\sin(\theta)}{\sinh(2kH)}\frac{\partial}{\partial x}\right)h, \tag{A 1b}$$

$$\mathscr{W}_{qo}o = -\frac{\partial}{\partial x}[|C_g|\sin(\theta)|A|^2 o] + |C_g|\cos(\theta)|A|^2\frac{\partial o}{\partial y}, \tag{A 1c}$$

$$\mathscr{W}_{qq}q = \frac{\partial}{\partial x}[|C_g|\cos(\theta)q] + |C_g|\sin(\theta)\frac{\partial q}{\partial y}, \tag{A 1d}$$

$$\mathscr{W}_{qh}h = -\left(\frac{\partial|C_g|}{\partial k}\frac{\partial k}{\partial H} + \frac{\partial|C_g|}{\partial H}\right)\sin(\theta)|A|^2\frac{\partial h}{\partial y} - \frac{\partial}{\partial x}\left[\left(\frac{\partial|C_g|}{\partial k}\frac{\partial k}{\partial H} + \frac{\partial|C_g|}{\partial H}\right)|A|^2\cos(\theta)h\right]. \tag{A 1e}$$

The linear coefficients for the linearized momentum, mass and bottom topography equation are

$$\mathscr{M}_{uu}u = -\frac{\hat{r}|u_w|}{H}u + \frac{\partial}{\partial x}\left[\left(-\frac{\partial\mathscr{G}}{\partial U} + U^{St}\right)u\right] - (V + V^{St})\frac{\partial}{\partial y}u, \tag{A 2a}$$

$$\mathscr{M}_{uv}v = fv + V^{St}\frac{\partial v}{\partial x} - \frac{\partial}{\partial x}\left[\frac{\partial\mathscr{G}}{\partial V}v\right], \tag{A 2b}$$

$$\mathscr{M}_{uz}z = -\frac{\hat{r}|u_w|U^{St}}{H^2}z - g\frac{\partial z}{\partial x}, \tag{A 2c}$$

$$\mathscr{M}_{uh}h = \left[-\frac{\hat{r}|u_w|U}{H^2} + \frac{\hat{r}U}{H}\left(\frac{\partial|u_w|}{\partial H} + \frac{\partial|u_w|}{\partial k}\frac{\partial k}{\partial H}\right) - \left(f + \frac{\partial V}{\partial x}\right)\left(\frac{\partial V^{St}}{\partial k}\frac{\partial k}{\partial H} + \frac{\partial V^{St}}{\partial H}\right)\right]h + \frac{\partial}{\partial x}\left[\left(\frac{\partial\mathscr{G}}{\partial k}\frac{\partial k}{\partial H} + \frac{\partial\mathscr{G}}{\partial H}\right)h\right], \tag{A 2d}$$

$$\mathscr{M}_{uo}o = \frac{\partial V^{St}}{\partial\theta}\left(f + \frac{\partial V}{\partial x}\right)o - \frac{\partial}{\partial x}\left[\frac{\partial \mathscr{G}}{\partial\theta}o\right], \tag{A 2e}$$

$$\mathscr{M}_{uq}q = -\frac{\hat{r}U}{H}\frac{\partial|u_w|}{\partial|A|^2}q + \frac{\partial V^{St}}{\partial|A|^2}\left(f + \frac{\partial V}{\partial x}\right)q - \frac{\partial}{\partial x}\left[\frac{\partial \mathscr{G}}{\partial|A|^2}q\right], \tag{A 2f}$$

$$\mathscr{M}_{vu}u = -\left(f + \frac{\partial V}{\partial x} + \left(\frac{\partial \mathscr{G}}{\partial U} - U^{St}\right)\frac{\partial}{\partial y}\right)u, \tag{A 2g}$$

$$\mathscr{M}_{vv}v = -\left(\frac{\hat{r}|u_w|}{H}v + \left(V + \frac{\partial \mathscr{G}}{\partial V}\right)\frac{\partial v}{\partial y}\right), \tag{A 2h}$$

$$\mathscr{M}_{vz}z = \left(\frac{\hat{r}|u_w|V}{H^2} - g\frac{\partial}{\partial y}\right)z, \tag{A 2i}$$

$$\mathscr{M}_{vh}h = \left[-\frac{\hat{r}V}{H}\left(\frac{|u_w|}{H} - \left(\frac{\partial|u_w|}{\partial H} + \frac{\partial|u_w|}{\partial k}\frac{\partial k}{\partial H}\right)\right) + \frac{\tau_y}{H^2} + \left(f + \frac{\partial V}{\partial x}\right)\left(\frac{\partial U^{St}}{\partial k}\frac{\partial k}{\partial H} + \frac{\partial U^{St}}{\partial H}\right) + \left(\frac{\mathscr{G}}{\partial k}\frac{\partial k}{\partial H} + \frac{\partial \mathscr{G}}{\partial H}\right)\frac{\partial}{\partial y}\right]h, \tag{A 2j}$$

$$\mathscr{M}_{vo}o = -\left(\frac{\partial U^{St}}{\partial\theta}\left(f + \frac{\partial V}{\partial x}\right) + \frac{\partial \mathscr{G}}{\partial\theta}\frac{\partial}{\partial y}\right)o, \tag{A 2k}$$

$$\mathscr{M}_{vq}q = -\frac{\hat{r}V}{H}\frac{\partial|u_w|}{\partial|A|^2}q - \left(\frac{\partial U^{St}}{\partial|A|^2}\left(f + \frac{\partial V}{\partial x}\right) + \frac{\partial \mathscr{G}}{\partial|A|^2}\frac{\partial}{\partial y}\right)q, \tag{A 2l}$$

$$\mathscr{M}_{zu}u = -\frac{\partial}{\partial x}\left[Hu\right], \quad \mathscr{M}_{zv}v = -\left(H\frac{\partial}{\partial y} + s\right)v, \quad \mathscr{M}_{zz}z = -\left(V + V^{St}\right)\frac{\partial z}{\partial y}, \tag{A 2m–o}$$

$$\mathscr{M}_{zh}h = s\left(\frac{\partial V^{St}}{\partial k}\frac{\partial k}{\partial H} + \frac{\partial V^{St}}{\partial H}\right)h + \frac{\partial}{\partial y}\left(\left(\frac{\partial V^{St}}{\partial k}\frac{\partial k}{\partial H} + \frac{\partial V^{St}}{\partial H}\right)H + V + V^{St}\right)h + \frac{\partial}{\partial x}\left[H\left(\frac{\partial U^{St}}{\partial k}\frac{\partial k}{\partial H} + \frac{\partial U^{St}}{\partial H}\right)h\right], \tag{A 2p}$$

$$\mathscr{M}_{zo}o = -\left(s\frac{\partial V^{St}}{\partial\theta} + H\frac{\partial V^{St}}{\partial\theta}\frac{\partial}{\partial y}\right)o - \frac{\partial}{\partial x}\left[H\frac{\partial U^{St}}{\partial\theta}o\right], \tag{A 2q}$$

$$\mathscr{M}_{zq}q = -\left(s\frac{\partial V^{St}}{\partial|A|^2} + H\frac{\partial V^{St}}{\partial|A|^2}\frac{\partial}{\partial y}\right)q - \frac{\partial}{\partial x}\left[H\frac{\partial U^{St}}{\partial|A|^2}q\right], \tag{A 2r}$$

$$\mathscr{M}_{hu}u = -\frac{\partial}{\partial x}[\left(c_b|u_w|^2 + c_s|u_w|^3H\right)u], \tag{A 2s}$$

$$\mathscr{M}_{hv}v = -\frac{\partial}{\partial y}[\left(c_b|u_w|^2 + c_s|u_w|^3H\right)v], \tag{A 2t}$$

$$\mathscr{M}_{hz}z = -\frac{\partial}{\partial y}c_s|u_w|^3(V + V^{St})z, \tag{A 2u}$$

$$\mathscr{M}_{hh}h = \frac{\partial}{\partial x}\left[(c_b|u_w|^2 + c_s|u_w|^3H)\left(\frac{\partial u^{St}}{\partial H} + \frac{\partial u^{St}}{\partial k}\frac{\partial k}{\partial H}\right)h + (c_b\lambda_b|u_w|^3 + c_s\lambda_s|u_w|^5)\frac{\partial h}{\partial x}\right] + \frac{\partial}{\partial y}\left[\left\{(V + V^{St})|u_w|^3 + (c_b|u_w|^2 + c_s|u_w|^3H)\left(\frac{\partial v^{St}}{\partial H} + \frac{\partial v^{St}}{\partial k}\frac{\partial k}{\partial H}\right)\right\}h + (c_b\lambda_b|u_w|^3 + c_s\lambda_s|u_w|^5)\frac{\partial h}{\partial y}\right], \tag{A 2v}$$

$$\mathscr{M}_{ho}o = -\frac{\partial}{\partial x}\left[(c_b|u_w|^2 + c_s|u_w|^3H)\frac{\partial u^{St}}{\partial o}o\right] - \frac{\partial}{\partial y}\left[(c_b|u_w|^2 + c_s|u_w|^3H)\frac{\partial v^{St}}{\partial o}o\right], \tag{A 2w}$$

$$\mathscr{M}_{hq}q = -\frac{\partial}{\partial x}\left[(c_b|u_w|^2 + c_s|u_w|^3H)\frac{\partial u^{St}}{\partial q}q\right] - \frac{\partial}{\partial y}\left[(c_b|u_w|^2 + c_s|u_w|^3H)\frac{\partial v^{St}}{\partial q}q\right], \tag{A 2x}$$

where $c_b = H_0/U_{w0}^2$ and $c_s = 1/U_{w0}^3$. Note that if we included the feedback from the bottom topography in the wave orbital velocity this would add a term

$$\frac{\partial}{\partial y}\left[(V + V^{St})(2c_b|u_w| + c_s 3|u_w|^2H)\left(\frac{\partial|u_w|}{\partial H} + \frac{\partial|u_w|}{\partial k}\frac{\partial k}{\partial H}\right)h\right] \tag{A3}$$

onto $\mathscr{M}_{hh}h$ and a term

$$-\frac{\partial}{\partial y}\left[(V + V^{St})(2c_b|u_w| + 3c_s|u_w|^2H)\frac{\partial|u_w|}{\partial|A|^2}q\right] \tag{A4}$$

onto $\mathscr{M}_{hq}q$.

## REFERENCES


Boyd, J. P. 1987 Orthogonal rational functions on a semi-infinite interval. *J. Comput. Phys.* **70**, 63–88.

Boyd, J. P. 1989 *Chebyshev and Fourier Spectral Methods*. Springer.

Boyd, J. P. 1996 Traps and snares in eigenvalue calculations with applications to pseudospectral computations of ocean tides in a basin bounded by meridians. *J. Comput. Phys.* **126**, 11–20.

Boyd, J. P., Rangan, C. & Bucksbaum, P. H. 2003 Pseudospectral methods on a semi-infinite interval with application to the hydrogen atom: a comparison of the mapped Fourier-sine method with Laguerre series and rational Chebyshev expansions. *J. Comput. Phys.* **188**, 56–74.

Calvete, D., Falques, A., de Swart, H. E. & Dodd, N. 1999 Non-linear modeling of shoreface-connected sand ridges. In *Proc. Coastal Sediments* (ed. N. C. Kraus & W. G. McDougal), pp. 1123–1138. American Society of Civil Engineers.

Calvete, D., Falques, A., de Swart, H. E. & Walgreen, M. 2001*a* Modelling the formation of shore connected sand ridges on storm dominated inner shelves. *J. Fluid Mech.* **441**, 169–193.

Calvete, D. & de Swart, H. E. 2003 A nonlinear model study on the long-term behaviour of shore-connected sand ridges. *J. Geophys. Res.* **108** (C5), 3169.

Calvete, D., de Swart, H. E. & Falques, A. 2002 Effect of depth dependent wave stirring on the final amplitude of shore-connected sand ridges. *Continent. Shelf Res.* **22**, 2763–2776.

Calvete, D., Walgreen, M., de Swart, H. E. & Falques, A. 2001*b* A model for sand ridges on the shelf: Effect of tidal and steady currents. *J. Geophys. Res.* **106** (C5), 9311–9325.

Csanady, G. T. 1982 *Circulation in the Coastal Ocean*. D. Reidel.

Duane, D. B., Field, M. E., Miesberger, E. P. & Swift, D. J. P. 1972 Linear shoals on the Atlantic continental shelf, Florida to Long Island. In *Shelf Sediment Transport: Process and Pattern* (ed. D. J. P. Swift, D. B. Duane & O. H. Pikey), pp. 447–498. Van Nostrand Reinhold.

Falques, A., Calvete, D. & Montoto, A. 1998*a* Bed-flow instabilities of coastal currents. In *Physics of Estuaries and Coastal Seas*, pp. 417–424. A. A. Balkema.

Falques, A., Calvete, D., de Swart, H. E. & Dodd, N. 1998*b* Morphodynamics of shoreface-connected ridges. In *Coastal Engineering* (ed. J. Dronkers & M. Scheffers), pp. 2851–2864. A. A. Balkema.

Huthnance, J. M. 1982 On the mechanism forming linear sand bars. *Estuarine, Coast. Shelf Sci.* **14**, 79–99.

Iranzo, V. & Falques, A. 1992 Some spectral approximations for differential equations in unbounded domains. *Computer Method. Appl. Mech. Engng* **98**, 105–126.

Lane, E. M., Restrepo, J. M. & McWilliams, J. C. 2007 Wave-current interaction: A comparison of radiation-stress and vortex-force representations. *J. Phys. Oceanogr.* (in press).

Lentz, S. J. 2001 The influence of stratification on the wind-driven cross-shelf circulation over the North Carolina shelf. *J. Phys. Oceanogr.* **31**, 2749–2760.

McClennen, C. E. & McMaster, R. L. 1971 Probable Holocene transgressive effects on the geomorphic features of the continental shelf off New Jersey, United States. *Mar. Sediments* **7**, 67–72.

McWilliams, J. C. & Restrepo, J. M. 1999 The wave-driven ocean circulation. *J. Phys. Oceanogr.* **29**, 2523–2540.

McWilliams, J. C., Restrepo, J. M. & Lane, E. M. 2004 Interaction of waves and currents in coastal waters: An asymptotic theory for the interaction of waves and currents in shallow coastal waters. *J. Fluid Mech.* **511**, 135–178.

van der Meene, J. W. H. 1996 Sediment structures of combined flow deposits from shoreface-connected rodgs along the central Dutch coast. *Mar. Geol.* **131**, 151–175.

Mei, C. C. 1989 *The Applied Dynamics of Ocean Surface Waves*. World Scientific.

Off, T. 1960 Rhythmic sand bodies caused by tidal currents. *Bull. Am. Assoc. Petrol. Geologists* **47**, 324–341.

Parker, G., Lanfredi, N. W. & Swift, D. J. P. 1982 Seafloor response to flow in the southern hemisphere sand-ridge field: Argentina inner shelf. *Sediment Geol.* **33**, 195–216.

Restrepo, J. M. 2001 Sediment dynamics and wave–current interactions. *Continent. Shelf Res.* **21**, 1331–1360.

Swift, D. J. P., Duane, D. B. & McKinney, T. F. 1973 Ridge and swale topography of the Middle Atlantic Bight, North America: secular response to the Holocene hydraulic regime. *Mar. Geol.* **15**, 227–247.

Swift, D. J. P., Holliday, B., Avignone, N. & Schideler, G. 1972 Anatomy of a shoreface ridge system, False Cape, Virginia. *Mar. Geol.* **12**, 59–84.

Swift, D. J. P., Parker, G., Lanfredi, N. W., Perillo, G. & Figge, K. 1978 Shoreface-connected sand ridges on American and European shelves: A comparison. *Estuarine Coast. Mar. Sci.* **7**, 257–273.

Trowbridge, J. H. 1995 A mechanism for the formation and maintenance of shore-oblique sand ridges on storm dominated shelves. *J. Geophys. Res.* **100** (C8), 16071–16086.

Walgreen, M., Calvete, D. & de Swart, H. E. 2002 Growth of large-scale bed forms due to storm driven and tidal currents: a model approach. *Continent. Shelf Res.* **22**, 2777–2793.

Walgreen, M., de Swart, H. E. & Calvete, D. 2003 Effect of grain size sorting on the formation of shoreface-connected sand ridges. *J. Geophys. Res.* **108** (C3), 3063S.

Walgreen, M., de Swart, H. E. & Calvete, D. 2004 A model for grain-size sorting over tidal sand ridges. *Ocean Dyn.* **54**, 374–384.